

Thermal fluctuations in shape, thickness, and molecular orientation in lipid bilayers

Max C. Watson, Evgeni S. Penev, Paul M. Welch, and Frank L. H. Brown

Citation: *J. Chem. Phys.* **135**, 244701 (2011); doi: 10.1063/1.3660673

View online: <http://dx.doi.org/10.1063/1.3660673>

View Table of Contents: <http://jcp.aip.org/resource/1/JCPSA6/v135/i24>

Published by the [American Institute of Physics](#).

Additional information on *J. Chem. Phys.*


Journal Homepage: <http://jcp.aip.org/>

Journal Information: http://jcp.aip.org/about/about_the_journal

Top downloads: http://jcp.aip.org/features/most_downloaded

Information for Authors: <http://jcp.aip.org/authors>

ADVERTISEMENT



AIP Advances

Special Topic Section:
PHYSICS OF CANCER

Why cancer? Why physics? [View Articles Now](#)

Thermal fluctuations in shape, thickness, and molecular orientation in lipid bilayers

Max C. Watson,^{1,a)} Evgeni S. Penev,^{2,b)} Paul M. Welch,³ and Frank L. H. Brown^{1,2,a)}

¹Department of Physics, University of California, Santa Barbara, California 93106, USA

²Department of Chemistry and Biochemistry, University of California, Santa Barbara, California 93106, USA

³Theoretical Division, Los Alamos National Laboratory, Los Alamos, New Mexico 87545, USA

(Received 19 July 2011; accepted 26 October 2011; published online 22 December 2011)

We present a unified continuum-level model for bilayer energetics that includes the effects of bending, compression, lipid orientation (tilting relative to the monolayer surface normal), and microscopic noise (protrusions). Expressions for thermal fluctuation amplitudes of several physical quantities are derived. These predictions are shown to be in good agreement with molecular simulations.

© 2011 American Institute of Physics. [doi:10.1063/1.3660673]

I. INTRODUCTION

As early as 1890, oscillations in the shape of red blood cells were observed with an ordinary microscope.¹ It was later shown that this “flicker effect” could be explained as a consequence of thermal fluctuations of the membrane surface.² Thermal fluctuations are implicated in a number of additional biophysical phenomena, including the steric repulsion between bilayers,^{3,4} cellular motility,⁵ and entropically driven interactions between integral proteins.^{6,7} In addition to these effects, analyzing thermal fluctuations allows one to gain insight into the structure and behavior of the membrane itself.

Traditional understanding of membrane deformations is rooted in the picture put forth by Helfrich⁸ and Canham,⁹ in which the membrane is modeled as a smooth, structureless sheet with energetic penalties due to bending and stretching. When a more detailed framework is needed, the molecular details of each monolayer also come into play. At the macroscopic level, liquid crystal theory tells us that the orientation of the lipids must be taken into account.¹⁰ On smaller length scales, the monolayer surfaces are no longer smooth, and are subject to molecular protrusions.^{11,12}

In terms of lipid orientation, generalization of the Helfrich energy enters in terms of molecular tilt.^{13,14} A lipid is considered tilted when the vector pointing along the hydrocarbon chain is not perpendicular to the monolayer-water interface. Hamm and Kozlov¹⁴ have derived an elastic theory for non-stretched monolayers, showing that a divergence in the tilt field is energetically equivalent to bending the membrane. The tilt degree of freedom is involved in many biological situations, including the formation of fusion stalks,¹⁵ the line tension between lipid domains,¹⁶ the orientation of cholesterol,^{17–19} the deformation energy due to transmembrane proteins,^{20–28} and the lipid-mediated interactions between proteins.^{25,27–29} Molecular orientation is also believed to play a role in certain non-biological phases. Unlike the fluid L_α phase, a non-vanishing average tilt is present in the in-

verted hexagonal H_{II} , inverted micellar cubic Q_{II} ,³⁰ and tilted gel $L_{\beta'}$ ³¹ phases. The tilt order parameter is believed to give rise to the rippled $P_{\beta'}$ phase.^{32–35}

On length scales shorter than the bilayer thickness, the monolayer-water interface can no longer be described by the Helfrich and Canham picture. The microscopic surface of an amphiphilic membrane constantly changes as the molecules bob in and out of the interfaces. These out of plane perturbations, known as protrusions, are traditionally associated with a hydrophobic energy due to the increased hydrocarbon-water contact area.^{11,12} The effect of protrusions has been measured in terms of micelle kinetics³⁶ and the repulsive force between membranes separated by small distances.^{3,37} The role of protrusions has also been discussed within the context of interfacial enzymes.³⁸

Molecular dynamics simulation has evolved as a method of connecting theoretical models with specific lipid bilayers and providing the values of material parameters through virtual experiments. Measurement of the height (undulation) fluctuations has become a standard method^{29,39–54} to calculate the bending rigidity of homogeneous fluid membranes. Analysis of thickness (peristaltic) fluctuations has also been conducted^{29,41–44,50} in order to extract the value of the area compressibility modulus. In Brannigan and Brown⁴⁴ (hereafter BB), a model was introduced to describe fluctuations in both height and thickness as well as the effect of protrusions. Recently, tilt fluctuations have also been measured by May, Narang, and Kopelevich^{52,53} (hereafter MNK) and described within the context of the Hamm and Kozlov theory.

In this paper, we present a model for membrane energetics that includes the effects of bending, thickness, tilt, and protrusions. We show that the entire range of behavior, including tilt, may be decoupled into peristaltic and undulation modes. In addition to height and thickness averages, expressions for the thermal fluctuations of various tilt-related quantities are also provided. In Fourier space, the tilt deformations may be further decomposed in terms of longitudinal and transverse modes. Analytic expressions for the fluctuation spectra show excellent agreement with two separate coarse-grained simulations: (i) an implicit solvent model which we have previously developed,⁴⁵ and (ii) the MARTINI force field for

^{a)} Authors to whom correspondence should be addressed. Electronic addresses: maxcw@physics.ucsb.edu and flbrown@chem.ucsb.edu.

^{b)} Present address: Department of Mechanical Engineering and Materials Science, Rice University, Houston, Texas 77005, USA.

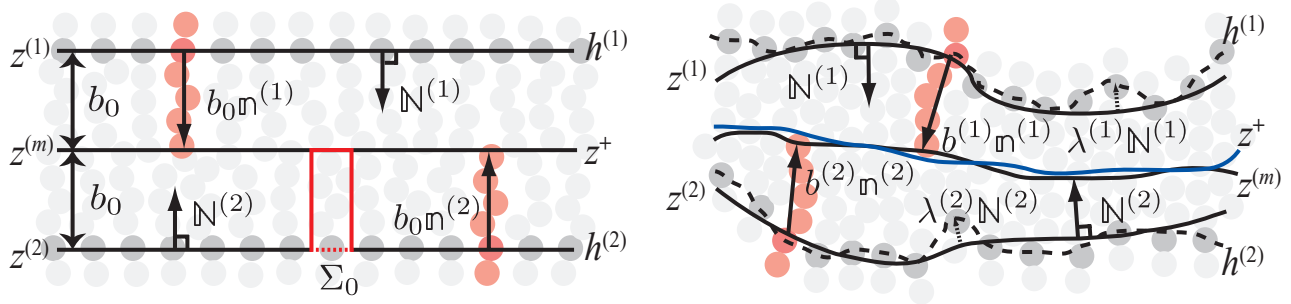


FIG. 1. For each lipid, dark gray circles mark the portion of the molecule separating the polar head from the hydrocarbon tails. On a coarse-grained level, the polar-nonpolar interfaces are described by $z^{(1)}$ and $z^{(2)}$. The unit vectors $\mathbf{N}^{(\alpha)}$ are normal to $z^{(\alpha)}$ and point toward the interior of the bilayer. The unit vectors field $\mathbf{m}^{(\alpha)}$ points along the hydrocarbon chains. $b^{(\alpha)}\mathbf{m}^{(\alpha)}$ extend from $z^{(\alpha)}$ to the surface separating the two leaflets, $z^{(m)}$. In other words, the top monolayer is bounded by $z^{(1)}$ and $z^{(m)}$, while the bottom monolayer is bounded by $z^{(m)}$ and $z^{(2)}$. The mean height z^+ is the average of $z^{(1)}$ and $z^{(2)}$. Left: a bilayer in its minimal energy configuration, in which $\lambda^{(\alpha)} = 0$, $z^{(m)} = z^+$, $\mathbf{N}^{(\alpha)} = \mathbf{n}^{(\alpha)} = 0$, the thickness is $2b_0$ and the area per molecule is Σ_0 (dotted red). The volume per lipid v satisfies $v = b_0\Sigma_0$. Since there are no protrusions, $h^{(\alpha)} = z^{(\alpha)}$. Right: an arbitrarily deformed bilayer. On short length scales, the polar-nonpolar interfaces $h^{(\alpha)}$ are not smooth (dashed curves). The protrusion fields $\lambda^{(\alpha)}$ displace the interface in the normal direction, so that $(-1)^\alpha \lambda^{(\alpha)}\mathbf{N}^{(\alpha)}$ (dashed vectors) extend from $z^{(\alpha)}$ to $h^{(\alpha)}$. The fields $z^{(m)}$ (black) and z^+ (blue) differ in general. The thickness deformations are exaggerated for illustrative purposes. We will assume throughout the paper that the absolute values of the following quantities are much less than one: $N_j^{(\alpha)}$, $n_j^{(\alpha)}$, $\nabla\mathbf{N}^{(\alpha)}$, $\nabla\mathbf{n}^{(\alpha)}$, $\nabla z^{(m)}$, $\Sigma^{(\alpha)}/\Sigma_0 - 1$, $b^{(\alpha)}/b_0 - 1$, $|z^{(\alpha)} - z^{(m)}|/b_0 - 1$, $(z^+ - z^{(m)})/b_0$, $\nabla\lambda^{(\alpha)}$, $\lambda^{(\alpha)}/b_0$.

dipalmitoylphosphatidylcholine (DPPC),^{55,56} which includes explicit water. By fitting our expressions to the simulation results, the values of the elastic constants may be extracted.

II. BILAYER ENERGETICS

In this section, we derive an expression for the total bilayer free energy \mathcal{F} as a local quadratic functional of multiple fields describing membrane “shape.” The approach we take is strongly motivated by the work of May and Ben-Shaul,^{21,22} in that we start with a deceptively simple-looking expression for the free energy per lipid motivated by the venerable opposing forces model¹² (see Eq. (11)) and construct the primary long-wavelength contributions to \mathcal{F} as the natural consequence of this model. We allow for quite general membrane deformations subject to the conservation of lipid volume (see Fig. 1), which represents a considerable generalization beyond the cylindrically symmetric and leaflet-symmetric deformations previously considered by May and Ben-Shaul. Additionally, we include energetic contributions due to inter-lipid twist^{10,14} (see Fig. 4) and molecular-scale protrusion effects that are absent from the opposing forces model.

The final outcome of the calculation outlined above is summarized in Eqs. (26)–(28). The various fields necessary to describe membrane shape and appearing in \mathcal{F} are defined and discussed in Sec. II A. Expressing \mathcal{F} in terms of these fields is a complicated geometric problem, even when truncating to second order in deviations from the flat ground state configuration. To simplify the presentation, we outline the steps necessary for this derivation in Secs. II B and II C, but leave many of the details to Appendix A.

We recognize that some readers will not be interested in the details of the theory and will want to skip ahead to the results. Practical expressions for the thermal fluctuation spectra of various measurable fields are presented in Eqs. (39)–(43) of Sec. III, which represent excellent approximations to the lengthy full expressions found in Appendix D (at least for the bilayers studied in this work). Tables I and II provide a listing

of all the symbols used throughout the text and should prove a useful resource to readers looking to understand the results of later sections without fully digesting the underlying theory.

A. GEOMETRIC DESCRIPTION

Throughout this paper, superscripts $\alpha = 1$ and $\alpha = 2$ will refer to the top and bottom leaflets of the bilayer, respectively. Vectors are written in two ways: \mathbf{c} denotes a three-dimensional vector while the two-dimensional vector \mathbf{c} refers to the xy components of \mathbf{c} . The vector calculus operations of divergence, gradient, and curl are only applied to vectors of the \mathbf{c} flavor and only act within the xy plane. Excluding Appendix C, the indices j and k each run over the x and y components of vectors. The quantity $\mathbf{r} = (x, y)$ denotes two-dimensional position.

The cross sectional area per lipid at the hydrocarbon-water interface that minimizes the monolayer free energy per molecule in a flat, tension-free geometry is denoted by Σ_0 . The corresponding average hydrocarbon chain length is given by b_0 . The fields $z^{(\alpha)}(\mathbf{r})$ describe the macroscopic surface separating the polar heads and hydrocarbon tails of each monolayer (Fig. 1). The surface separating the top and bottom monolayers is denoted by $z^{(m)}(\mathbf{r})$. For later convenience, we shall define

$$\begin{aligned} z^+ &\equiv \frac{z^{(1)} + z^{(2)}}{2}, \\ z^- &\equiv \frac{z^{(1)} - z^{(2)} - 2b_0}{2}, \\ \varepsilon &\equiv z^{(m)} - z^+. \end{aligned} \quad (1)$$

Here z^+ describes the undulations of the bilayer, averaged over the top and bottom leaflets. z^+ is analogous to the field used by Helfrich⁸ to describe membrane shape. Deviations from the mean membrane thickness are described by z^- . We shall more succinctly refer to z^+ and z^- as the mean height and deviations in thickness, respectively. Deviations of $z^{(m)}$

TABLE I. The list of fields associated with the bilayer along with the equation or figure where they are first defined. The superscript $\alpha = \{1, 2\}$ refers to the top and bottom leaflets, respectively. Though the list is long, the only fields present in the final expression for the bilayer free energy (Eqs. (26)–(28)) are $\{z^\pm, \lambda^\pm, \hat{\mathbf{m}}, \bar{\mathbf{m}}\}$.

Symbol	Definition	Symbol	Definition
Macroscopic fields		Protrusion fields	
$z^{(\alpha)}$	Hydrocarbon-water surfaces (Fig. (1))	$\lambda^{(\alpha)}$	Protrusion field for each monolayer (Fig. 1)
z^+	Mean bilayer height (Eq. (1))	λ^\pm	Antisymmetric/symmetric parts of $\lambda^{(\alpha)}$ (Eq. (7))
z^-	Deviations in bilayer thickness (Eq. (1))	$\Delta A^{(\alpha)}$	Relative area created by protrusions (Eq. (24))
$z^{(m)}$	Surface separating the two leaflets (Fig. 1)	Measured fields	
ε	Deviations of $z^{(m)}$ from z^+ (Eq. (1))	$h^{(\alpha)}$	Hydrocarbon-water surfaces (Fig. 1)
$b^{(\alpha)}$	Lipid chain length (Eq. (6))	h	Mean bilayer height (Eq. (8))
$\mathbb{N}^{(\alpha)}$	Vectors normal to $z^{(\alpha)}$ (Fig. 1)	t	Deviations in bilayer thickness (Eq. (8))
$\mathbf{N}^{(\alpha)}$	xy components of $\mathbb{N}^{(\alpha)}$	$\bar{\mathbf{m}}^{(\alpha)}$	Monolayer directors (Fig. 2)
$\mathbf{m}^{(\alpha)}$	Monolayer directors (Fig. 1)	$\bar{\mathbb{N}}^{(\alpha)}$	Vectors normal to $h^{(\alpha)}$ (Fig. 2)
$\mathbf{n}^{(\alpha)}$	xy components of $\mathbf{m}^{(\alpha)}$	$\bar{\mathbf{N}}^{(\alpha)}$	xy components of $\bar{\mathbb{N}}^{(\alpha)}$
$\mathbb{m}^{(\alpha)}$	Monolayer tilt (Eq. (4))	$\bar{\mathbb{m}}^{(\alpha)}$	Monolayer tilt (Eq. (9))
$\mathbf{m}^{(\alpha)}$	xy components of $\mathbb{m}^{(\alpha)}$	$\bar{\mathbf{m}}^{(\alpha)}$	xy components of monolayer tilt (Eq. (9))
$\hat{\mathbf{m}}, \bar{\mathbf{m}}$	Antisymmetric/symmetric tilt (Eq. (5))	$\hat{\mathbf{p}}, \bar{\mathbf{p}}$	Antisymmetric/symmetric tilt (Eq. (10))
$\hat{m}_q, \bar{m}_q^\perp$	Longitudinal and transverse	$\hat{p}_q^\parallel, \hat{p}_q^\perp$	Longitudinal and transverse
$\bar{m}_q^\parallel, \bar{m}_q^\perp$	components of $\hat{\mathbf{m}}_q$ and $\bar{\mathbf{m}}_q$ (Eqs. (31) and (32))	$\bar{p}_q^\parallel, \bar{p}_q^\perp$	components of $\hat{\mathbf{p}}_q$ and $\bar{\mathbf{p}}_q$ (Eqs. (40)–(43))
$\Sigma^{(\alpha)}$	Area per molecule at $z^{(\alpha)}$ (Eq. (11))	P_{xy}	xy -component of stress tensor (Eq. (45))
$\Sigma_h^{(\alpha)}$	Area per molecule at head group surfaces (Eq. (11))	$s(z)$	Stress profile (Eq. (45))
$\varepsilon_V^{(\alpha)}$	Effective monolayer thickness (Eq. (14))		
$\varepsilon_A^{(\alpha)}$	Area element at $z^{(\alpha)}$ (Eq. (A2))		

from the average shape z^+ are described in terms of ε . Both z^-/b_0 and ε/b_0 are assumed to be small quantities.

For a given leaflet, the macroscopic tilt vector \mathbb{m} has been defined as¹³

$$\mathbb{m} \equiv \frac{\mathbf{m}}{\mathbf{m} \cdot \mathbb{N}} - \mathbb{N}, \quad (2)$$

where \mathbf{m} , known as the director, is the unit vector pointing from the polar head along the hydrocarbon chain. Here, the unit normal to the surface \mathbb{N} points toward the interior of the membrane. Note that \mathbb{m} is exactly parallel to the interface ($\mathbb{m} \cdot \mathbb{N} = 0$), and its length is equal to the tangent of the angle θ between \mathbf{m} and \mathbb{N} ; \mathbb{m} is not a unit vector.

In practice, we work with the macroscopic tilt vectors $\mathbb{m}^{(\alpha)}$ in the following way. We assume $\partial z^{(\alpha)}/\partial x \ll 1$ and $\partial z^{(\alpha)}/\partial y \ll 1$. Up to first order, the vectors normal to $z^{(\alpha)}$ are

$$\mathbb{N}^{(1)} = (\nabla z^{(1)}, -1), \quad \mathbb{N}^{(2)} = (-\nabla z^{(2)}, 1). \quad (3)$$

For each monolayer, the lipid orientation is described by $\mathbf{m}^{(\alpha)}$. At each point, we assume the angle θ between $\mathbf{m}^{(\alpha)}$ and $\mathbb{N}^{(\alpha)}$ is small. The xy components of the tilt vector may then be approximated as

$$\mathbf{m}^{(\alpha)} = \mathbf{n}^{(\alpha)} - \mathbf{N}^{(\alpha)}, \quad (4)$$

which is consistent with Eq. (2) up to first order in θ . This expression will serve as our working definition of the tilt vector. The z component is unnecessary since $|\mathbb{m}^{(\alpha)}|^2 \approx |\mathbf{m}^{(\alpha)}|^2$ up to second order in $\{\mathbf{N}^{(\alpha)}, \mathbf{n}^{(\alpha)}\}$. Later, it will be convenient to describe lipid orientation in terms of

$$\bar{\mathbf{m}} \equiv \frac{\mathbf{m}^{(1)} + \mathbf{m}^{(2)}}{2}, \quad \hat{\mathbf{m}} \equiv \frac{\mathbf{m}^{(1)} - \mathbf{m}^{(2)}}{2}, \quad (5)$$

since we will show that \mathcal{F} is block diagonal—the fields $\{z^+, \hat{\mathbf{m}}, \varepsilon\}$ are decoupled from the fields $\{z^-, \bar{\mathbf{m}}\}$.

The effective lipid chain length is described by $b^{(\alpha)}$. By effective length, we mean the distance from the hydrocarbon interface to the end of the tail, as measured by a straight line. We assume no voids exist within the membrane, so $b^{(\alpha)\mathbb{m}^{(\alpha)}}$ is required to extend from $z^{(\alpha)}$ to $z^{(m)}$ (Fig. 1). Up to first order in the small quantities $\{\mathbf{n}^{(\alpha)}, \nabla z^{(m)}, |z^{(\alpha)} - z^{(m)}|/b_0 - 1\}$, we have

$$b^{(1)} = z^{(1)} - z^{(m)} \quad b^{(2)} = z^{(m)} - z^{(2)}. \quad (6)$$

As mentioned in the Introduction, the polar-nonpolar interfaces are subject to microscopic displacements from the $z^{(\alpha)}$ fields, or protrusions $\lambda^{(\alpha)}$ at short length scales. The actual position of each interface is denoted by $h^{(\alpha)}$ (Fig. 1). Though the protrusions are formally considered to displace the interface normal to $z^{(\alpha)}$, they point solely in the z direction up to first order in $\{\mathbf{N}^{(\alpha)}, \lambda^{(\alpha)}/b_0\}$, such that $h^{(\alpha)} = z^{(\alpha)} + \lambda^{(\alpha)}$. For both leaflets, a protrusion in the positive z direction corresponds to $\lambda^{(\alpha)} > 0$ in our convention. Just like $z^{(\alpha)}$, $\lambda^{(\alpha)}$ may be decomposed into symmetric and antisymmetric parts,

$$\lambda^+ \equiv \frac{\lambda^{(1)} + \lambda^{(2)}}{2}, \quad \lambda^- \equiv \frac{\lambda^{(1)} - \lambda^{(2)}}{2}. \quad (7)$$

The mean height h of the bilayer and deviations in the bilayer thickness t are directly measured in our simulations. Up to linear order in $\{\nabla \lambda^{(\alpha)}, \mathbf{N}^{(\alpha)}, \lambda^{(\alpha)}/b_0\}$, we have

$$h \equiv z^+ + \lambda^+, \quad t \equiv z^- + \lambda^-. \quad (8)$$

Only first order contributions are significant since we will be measuring thermal averages quadratic in h and t . From a theoretical perspective, we imagine these fields to reflect precisely defined interfaces between the hydrocarbon chains and surrounding water. In practice, these fields are extracted from the

TABLE II. List of symbols along with the equation or figure where they are defined. Note that all elastic constants are defined as monolayer properties and that we define c_0 to be the spontaneous *total* curvature of the monolayer and choose its sign such that $c_0 > 0$ implies lipids with a preference for micelle over reverse micelle geometries. These conventions agree with some works and differ from others; extreme care must be exercised in comparing to prior results. (In particular, the conventions used in BB differ from those introduced here for the quantities k_A , k_c^b , and c_0 . In BB, k_A and k_c refer to bilayer properties and correspond to double the values defined here. c_0 in BB is defined as the monolayer *mean* curvature and corresponds to half the value defined here.)

Symbol	Definition	Symbol	Definition
\mathbf{q}	Wave number (q_x, q_y) (Eq. (29))	Monolayer Constants	
\mathbf{r}	xy position (Eq. (14))	b_0	Average monolayer thickness (Fig. 1)
M	Index of highest wave number (Eq. (29))	d	Distance from $z^{(m)}$ to the neutral surface (Eq. (23))
\mathbf{g}_q	Fourier trans. of some function $\mathbf{g}(\mathbf{r})$ (Eq. (29))	Σ_0	Average cross sectional area per lipid (Fig. 1)
L	System size (Eq. (29))	v	Volume per lipid, $v = b_0 \Sigma_0$ (Eq. (14))
Free Energies		c_0	Monolayer spontaneous total curvature (Eq. (12)), (twice the spontaneous mean curvature)
$\check{f}^{(\alpha)}$	Macroscopic energy per lipid (Eq. (11))	k_c^Σ	Splay (bending) modulus at constant area, (Eq. (12))
$f_{\text{plane}}^{(\alpha)}$	Macroscopic energy density in xy plane (Eq. (14))	k_c^b	Splay (bending) mod. at const. chain length, (Eq. (19))
$f_{\text{p}}(z^-, \hat{\mathbf{m}})$	Macroscopic energy density in xy plane from	k_c	Splay (bending) modulus at neutral surface (Eq. (22))
$f_{\text{u}}(z^+, \hat{\mathbf{m}}, \varepsilon)$	peristaltic(p)/undulation(u) modes (Eqs. (19) and (20))	k_G	Saddle-splay (Gaussian curvature) modulus (Eq. (12))
$f_{\text{p}}(z^-, \hat{\mathbf{m}}, \lambda^-)$	Total energy density in xy plane from	k_A	Compressibility modulus (Eq. (12))
$f_{\text{u}}(z^+, \hat{\mathbf{m}}, \lambda^+)$	peristaltic(p)/undulation(u) modes (Eqs. (27) and (28))	μ	Cross-term modulus for $\check{f}^{(\alpha)}$ (Eq. (12))
F	Total macroscopic free energy (Eq. (18))	Ω	Cross-term modulus for $f_{\text{plane}}^{(\alpha)}$ (Eq. (19))
\mathcal{F}	Total free energy (Eq. (26))	κ_θ	Tilt modulus (Eq. (12))
$\mathcal{F}_{\text{p}}, \mathcal{F}_{\text{u}}$	Total peristaltic(p)/undulation(u) energy (Eqs. (27) and (28))	κ_{tw}	Twist modulus (Eq. (13))
Abbreviations		ζ	Constant term in $\check{f}^{(\alpha)}$ (Eq. (12))
BB	Brannigan and Brown ⁴⁴	γ_λ	Protrusion-related surface tension (Eq. (25))
MNK	May, Narang and Kopelevich ^{52,53}	k_λ	Hookean protrusion coefficient (Eq. (25))
CG	Coarse-Grained implicit solvent model ⁴⁵	B	Head group repulsion coefficient (Eq. (11))
DPPC	MARTINI force field for DPPC ^{55,56}	γ_s	Surface tension at the $z^{(\alpha)}$ surfaces (Eq. (11))
		τ	Hookean chain-stretching coefficient (Eq. (11))
		ℓ_c	Preferred lipid chain length (Eq. (11))
		ℓ_h	Distance from $z^{(\alpha)}$ to head groups (Eq. (A6))

simulation by measuring the positions of the interface points for each lipid (see Sec. V).

Like the height and thickness variables, the values of the tilt vectors measured in the simulation $\tilde{\mathbf{m}}^{(\alpha)}$ are a sum of both macroscopic and protrusion-related contributions. Strictly speaking, protrusions affect the measured value of the director fields $\tilde{\mathbf{m}}^{(\alpha)}$ as well as the measured normal vectors $\tilde{\mathbf{N}}^{(\alpha)}$ (Fig. 2). The resulting tilt vectors are given by $\tilde{\mathbf{m}}^{(\alpha)} = \tilde{\mathbf{m}}^{(\alpha)} - \tilde{\mathbf{N}}^{(\alpha)}$ with $|\tilde{\mathbf{m}}^{(\alpha)}|^2 \approx |\tilde{\mathbf{m}}^{(\alpha)}|^2$. Within our model, a protrusion changes the location of the polar-nonpolar interface while leaving the rest of the lipid in its original position. The measured director $\tilde{\mathbf{m}}^{(\alpha)}$ points from the protruded interface toward the end of the hydrocarbon chains. For the top layer, for example,

$$\tilde{\mathbf{m}}^{(1)} = \frac{b^{(1)}\mathbf{m}^{(1)} + \lambda^{(1)}\mathbf{N}^{(1)}}{|b^{(1)}\mathbf{m}^{(1)} + \lambda^{(1)}\mathbf{N}^{(1)}|}.$$

Up to linear order in $\{\lambda^{(\alpha)}/b_0, \mathbf{N}^{(\alpha)}, \mathbf{n}^{(\alpha)}\}$, we have $\tilde{\mathbf{m}}^{(\alpha)} = \mathbf{m}^{(\alpha)}$ (Fig. 2 (top)). Unlike the directors, $\tilde{\mathbf{N}}^{(\alpha)}$ is affected by gradients in the local protrusion field (Fig. 2 (bottom)). To first order in $\{\nabla\lambda^{(\alpha)}, \mathbf{N}^{(\alpha)}\}$, the measured normal vector is given by

$$\tilde{\mathbf{N}}^{(\alpha)} = \mathbf{N}^{(\alpha)} - (-1)^\alpha \nabla\lambda^{(\alpha)}.$$

The measured tilt vectors are then

$$\tilde{\mathbf{m}}^{(1)} = \mathbf{m}^{(1)} - \nabla\lambda^{(1)}, \quad \tilde{\mathbf{m}}^{(2)} = \mathbf{m}^{(2)} + \nabla\lambda^{(2)}. \quad (9)$$

It will also be useful to work with the symmetric and antisymmetric measured tilt vectors:

$$\bar{\mathbf{p}} \equiv \tilde{\mathbf{m}} - \nabla\lambda^-, \quad \hat{\mathbf{p}} \equiv \tilde{\mathbf{m}} - \nabla\lambda^+. \quad (10)$$

In what follows, we derive the bilayer free energy due to smooth macroscopic deformations as well as the additional free energy density due to microscopic protrusions.

B. Macroscopic bilayer free energy

We begin by introducing a monolayer free energy per molecule $\check{f}^{(\alpha)}$, which does not include the effect of protrusions. Our derivation is similar to that in May and Ben-Shaul,^{21,22} where the free energy density of the bilayer is obtained from a simple model of the free energy per molecule by means of geometric transformations. This approach differs from the original works of Frank¹⁰ and Helfrich,⁸ in which a Hamiltonian is derived based on symmetry arguments alone. However, it will be shown that our general expression for the macroscopic free energy (Eq. (12)) reduces back to past results in limiting cases.

The free energy per lipid is assumed to be of the phenomenological form

$$\check{f}^{(\alpha)} = \gamma_s \Sigma^{(\alpha)} + \frac{B}{\Sigma_h^{(\alpha)}} + \tau(b^{(\alpha)} - \ell_c)^2, \quad (11)$$

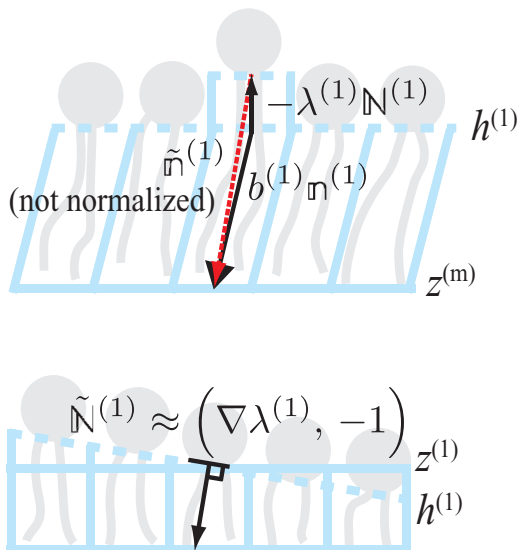


FIG. 2. Top: The hydrocarbon-water interface of the middle lipid is protruded upwards ($\lambda^{(1)} > 0$). The measured director $\tilde{\mathbf{m}}^{(1)}$ points from the displaced surface toward the end of the hydrocarbon chain (along the red dashed vector). The dashed vector only shows the direction of $\tilde{\mathbf{m}}^{(1)}$ but not its magnitude, since $\tilde{\mathbf{m}}^{(1)}$ is a unit vector. The monolayer thickness is large compared to $\lambda^{(1)}$, so $\tilde{\mathbf{m}}^{(1)} \approx \mathbf{m}^{(1)}$. Bottom: $\tilde{\mathbf{N}}^{(1)} \neq \mathbf{N}^{(1)}$ due to a gradient in the protrusion field.

where $\Sigma^{(\alpha)}$ and $\Sigma_h^{(\alpha)}$ are the molecular cross sectional area at the hydrocarbon-water interface and head group region, respectively (see Fig. 3). The first term reflects the energetic cost of exposing hydrocarbon chains to the aqueous solution. The surface tension γ_s is expected to lie between 20 and 50 mN/m.¹² The head groups repel each other, and are assumed to only interact within a given surface located at a fixed distance, ℓ_h , above the polar-nonpolar interface. In general, the repulsion is due to several effects, including electrostatics, steric forces, and hydration forces. In the well-known opposing forces model,¹² these contributions are incorporated through the term in $\tilde{f}^{(\alpha)}$ proportional to $1/\Sigma_h^{(\alpha)}$. The third term accounts for the lipid chain's conformational free energy with τ representing an entropic spring constant and ℓ_c is the preferred length. Only deformations that conserve volume of the lipid chain are allowed as it is assumed that the hydrocarbon core of the monolayer is effectively incompressible.

By applying geometric arguments detailed in Appendix A, Eq. (11) may be expressed to quadratic order in $\{\Sigma^{(\alpha)}/\Sigma_0 - 1, \mathbf{n}^{(\alpha)}, \mathbf{m}^{(\alpha)}\}$ while holding the volume per lipid constant. Introducing standard notations for the coefficients (see Appendix A to relate these constants to the parameters of the opposing forces model), we find

$$\begin{aligned} \frac{\tilde{f}^{(\alpha)}}{\Sigma_0} &= \frac{k_A}{2} \left(\frac{\Sigma^{(\alpha)} - \Sigma_0}{\Sigma_0} \right)^2 + \frac{k_c^\Sigma}{2} (-\nabla \cdot \mathbf{n}^{(\alpha)} - c_0)^2 \\ &+ \mu \left(\frac{\Sigma^{(\alpha)} - \Sigma_0}{\Sigma_0} \right) \nabla \cdot \mathbf{n}^{(\alpha)} + k_G \det \left(\frac{\partial n_j^{(\alpha)}}{\partial r_k} \right) \\ &+ \frac{\kappa_\theta}{2} |\mathbf{m}^{(\alpha)}|^2 + \zeta. \end{aligned} \quad (12)$$

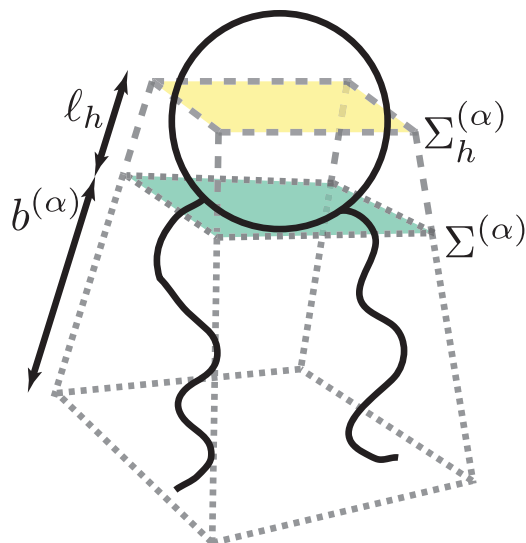


FIG. 3. The starting point of our model is the phenomenological macroscopic free energy per lipid $\tilde{f}^{(\alpha)}$,^{21,22} which is a function of the hydrocarbon chain length $b^{(\alpha)}$, the cross sectional area at the polar-nonpolar interface $\Sigma^{(\alpha)}$ (green), and the cross sectional area at the center of the head group $\Sigma_h^{(\alpha)}$ (yellow). The two surfaces which contain $\Sigma^{(\alpha)}$ and $\Sigma_h^{(\alpha)}$ are separated by a fixed distance ℓ_h . The volume v of the hydrocarbon chain region (finely dashed box) is constant to enforce chain incompressibility.

In writing this expression, we have used the relation $\gamma_s \Sigma_0 = B/\Sigma_0 + 2b_0\tau(b_0 - \ell_c)$, which follows from the requirement that $\Sigma^{(\alpha)} = \Sigma_h^{(\alpha)} = \Sigma_0$ represents the minimum free energy configuration of Eq. (11) when considering flat monolayer geometries that satisfy $\Sigma^{(\alpha)} = \Sigma_h^{(\alpha)} = v/b^{(\alpha)}$.

Before proceeding further, we note that two contributions to this expression vanish for the systems we will consider in this paper. First, the term containing k_G is related to Gaussian curvature and may be re-written as the divergence of a vector field:⁵⁷

$$\det \left(\frac{\partial n_j^{(\alpha)}}{\partial r_k} \right) = \frac{1}{2} \nabla \cdot [(\nabla \cdot \mathbf{n}^{(\alpha)}) \mathbf{n}^{(\alpha)} - (\mathbf{n}^{(\alpha)} \cdot \nabla) \mathbf{n}^{(\alpha)}].$$

Integrating this contribution over an area (as we will do below) merely results in a boundary term. We shall focus on homogeneous membranes with periodic boundary conditions, so that this term vanishes. Second, in order to compare our predictions with previous theoretical investigations, we will restrict the study to the case of vanishing lipid chemical potential. The constant contribution to Eq. (12), $k_c^\Sigma c_0^2/2 + \zeta$, is the lipid chemical potential divided by Σ_0 and we henceforth set this quantity to zero. It should be stressed that the simulations we shall eventually compare to are not carried out at constant vanishing chemical potential, but rather under the more computationally convenient condition of constant lipid number and vanishing applied surface tension. This is a possible source of concern that has seen substantial prior discussion in the literature.^{50,58-63} However, recent work suggests that the two conditions (vanishing chemical potential versus vanishing imposed tension) are consistent with one another, at least to the level of accuracy associated with our quadratic model.⁶⁴

The first term in Eq. (12) is associated with deviations in the area per molecule away from its mean value. The second term corresponds to deviations of the total effective curvature $-\nabla \cdot \mathbf{n}^{(\alpha)}$ from the total spontaneous curvature c_0 . This contribution is identical to the splay energy in nematic liquid crystal theory.¹⁰ The sign convention guarantees that a negative divergence in $\mathbf{n}^{(\alpha)}$, corresponding to a micelle shape, results in a positive curvature for either monolayer and that a positive value of the spontaneous curvature indicates lipids with a preference for micelle morphologies (note that within some conventions, the constant inside the splay energy is called $2c_0$ and/or may involve a sign difference from our definition. See the discussion in the caption of Table II). The symbol k_c^Σ reflects the cost of bending when the interfacial area per molecule $\Sigma^{(\alpha)}$ is held equal to its equilibrium value Σ_0 . The third term couples stretching/compression with curvature. The fourth term corresponds to the effective Gaussian curvature, or saddle-splay. As mentioned in the previous paragraph, this contribution vanishes for the cases considered herein. The final contribution is associated with molecular tilt. Note that in the limit $\kappa_\theta \rightarrow \infty$, $\mathbf{m}^{(\alpha)} = 0$ and we have $\nabla \cdot \mathbf{n}^{(\alpha)} = \pm \nabla^2 z^{(\alpha)}$ (see Eqs. (3) and (4)). The free energy then reduces to the more traditional Helfrich form.⁶⁵ A physical interpretation of the tilt term is given in Appendix B.

Although the modified opposing forces model (Eq. (11)) captures several contributions to the free energy, it does not account for the interactions between neighboring hydrocarbon chains. This may be included through the twist energy, which is well known within the liquid crystal literature.¹⁰ As shown in Fig. 4, twist corresponds to a specific type of variation in the tilt field. Unlike dilation, splay and tilt, twist is mainly associated with interactions between neighboring chains of lipids. It has been predicted that such deformations are energetically less costly.¹⁷ In Sec. V, we find that this is indeed the case. For a non-stretched monolayer ($\Sigma^{(\alpha)} = \Sigma_0$) Hamm and Kozlov¹⁴ showed that twist may be accounted for by adding a term proportional to $(\nabla \times \mathbf{m}^{(\alpha)})^2$ to the monolayer free energy. It has been shown using both elastic theory¹⁴ and symmetry arguments^{10,27} that the twist contribution is decoupled from the rest of the Hamiltonian. For the quasi two-dimensional membranes within our model, the twist term reduces to $(\partial m_x^{(\alpha)}/\partial y - \partial m_y^{(\alpha)}/\partial x)^2$. From Eq. (12), the free energy per molecule becomes

$$\begin{aligned} \frac{\check{f}^{(\alpha)}}{\Sigma_0} = & \frac{k_A}{2} \left(\frac{\Sigma^{(\alpha)} - \Sigma_0}{\Sigma_0} \right)^2 + \frac{k_c^\Sigma}{2} (\nabla \cdot \mathbf{n}^{(\alpha)})^2 \\ & + k_c^\Sigma c_0 \nabla \cdot \mathbf{n}^{(\alpha)} + \mu \left(\frac{\Sigma^{(\alpha)} - \Sigma_0}{\Sigma_0} \right) \nabla \cdot \mathbf{n}^{(\alpha)} \\ & + \frac{\kappa_\theta}{2} |\mathbf{m}^{(\alpha)}|^2 + \frac{\kappa_{tw}}{2} (\nabla \times \mathbf{m}^{(\alpha)})^2, \end{aligned} \quad (13)$$

where κ_{tw} is the twist modulus and we have explicitly removed the terms involving chemical potential and Gaussian curvature as previously discussed.

In addition to the orientational effects of splay, saddle-splay, and twist, the Frank free energy of liquid crystals also

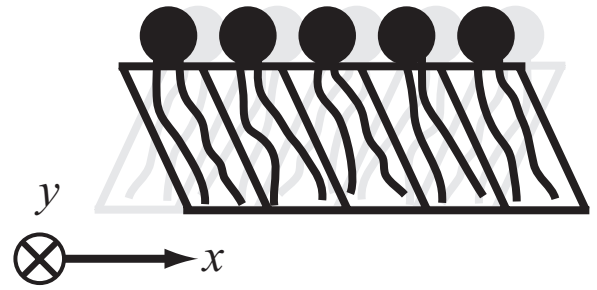


FIG. 4. Here, two neighboring rows of lipids have different values of $\mathbf{m}^{(\alpha)}$. Twist is present since the tilt vectors point in the x direction, but vary in the y direction. Thus, the κ_θ and κ_{tw} terms in Eq. (13) are nonzero.

includes a final “bend” term in the Hamiltonian^{10,14} (“bend” has a different meaning than in the membrane literature). For the lamellar phase, this would reflect interactions between opposing leaflets.³⁵ Its effect is expected to be even weaker than that of twist, since only the ends of lipids in opposing layers are in contact with each other. In terms of our quadratic Hamiltonian, we consider the free energy associated with intermonolayer coupling to be negligible. In Sec. V, we demonstrate that this assumption is valid. We will now use Eq. (13) to calculate the free energy density of a bilayer.

The total deformation energy is the sum over all molecules²¹

$$F = \int \check{f}^{(1)} dn^{(1)} + \int \check{f}^{(2)} dn^{(2)}.$$

The quantity $dn^{(\alpha)}$ is the number of lipids whose polar-nonpolar interfaces are located within the area element $d\mathbf{r} = dx dy$ as measured at $z^{(\alpha)}$. Each monolayer’s energy density projected onto the xy plane, $f_{\text{plane}}^{(\alpha)}$, satisfies

$$\int \check{f}^{(\alpha)} dn^{(\alpha)} = \frac{1}{v} \int \check{f}^{(\alpha)} g_V^{(\alpha)} d\mathbf{r} \equiv \int f_{\text{plane}}^{(\alpha)} d\mathbf{r}, \quad (14)$$

where the monolayer volume element $v dn^{(\alpha)} = dV^{(\alpha)} = g_V^{(\alpha)} d\mathbf{r}$. The condition $dV^{(\alpha)} = v dn^{(\alpha)}$ enforces constant volume per lipid^{21,22} (though this incompressibility condition is valid within the continuum regime, it breaks down on length scales comparable to the bilayer thickness (see Sec. II C)). The total macroscopic bilayer energy may then be written as an integral over the xy plane:

$$F = \int f_{\text{plane}}^{(1)} d\mathbf{r} + \int f_{\text{plane}}^{(2)} d\mathbf{r}. \quad (15)$$

The effective thickness $g_V^{(\alpha)}$ has been calculated previously in the context of protein inclusions,^{21,22} where the symmetric bilayer possessed cylindrical symmetry. In Appendix A, we derive the general expression for $g_V^{(\alpha)}$ where no symmetries are assumed (see Eq. (A1)). Since no constant terms are present in Eq. (13), only terms in $g_V^{(\alpha)}$ up to first order are needed for calculating $f_{\text{plane}}^{(\alpha)}$ to second order:

$$g_V^{(\alpha)} = b_0 + (-1)^\alpha \varepsilon + z^- + \frac{b_0^2}{2} \nabla \cdot \mathbf{n}^{(\alpha)}. \quad (16)$$

The energy density in the xy plane $f_{\text{plane}}^{(\alpha)}$ may be expressed in terms of monolayer thickness using the first order expression

for $\Sigma^{(\alpha)}$ (see Appendix A) combined with Eqs. (1) and (6):

$$\frac{\Sigma^{(\alpha)} - \Sigma_0}{\Sigma_0} = -\frac{z^-}{b_0} - (-1)^\alpha \frac{\varepsilon}{b_0} - \frac{b_0}{2} \nabla \cdot \mathbf{n}^{(\alpha)}. \quad (17)$$

Using Eqs. (1), (3), (4) and (13)–(17), the macroscopic bilayer free energy may be written as a functional of the various shape fields $F[z^{(1)}, z^{(2)}, \mathbf{m}^{(1)}, \mathbf{m}^{(2)}, \varepsilon]$. Though the full expression is lengthy, the result is most concisely described in terms of peristaltic $f_p(z^-, \hat{\mathbf{m}})$ and undulation $f_u(z^+, \hat{\mathbf{m}}, \varepsilon)$ contributions, which are decoupled from one another:

$$F = \int (f_p(z^-, \hat{\mathbf{m}}) + f_u(z^+, \hat{\mathbf{m}}, \varepsilon)) \, d\mathbf{r}, \quad (18)$$

where

$$\begin{aligned} f_p(z^-, \hat{\mathbf{m}}) &= \frac{k_A}{b_0^2} (z^-)^2 + k_c^b (\nabla^2 z^- + \nabla \cdot \hat{\mathbf{m}})^2 \\ &+ 2k_c^\Sigma c_0 (\nabla \cdot \hat{\mathbf{m}} + \nabla^2 z^-) + \frac{\Omega}{b_0} (\nabla \cdot \hat{\mathbf{m}} + \nabla^2 z^-) z^- \\ &+ \kappa_\theta \hat{\mathbf{m}}^2 + \kappa_{tw} (\nabla \times \hat{\mathbf{m}})^2, \end{aligned} \quad (19)$$

and

$$\begin{aligned} f_u(z^+, \hat{\mathbf{m}}, \varepsilon) &= k_c^b (\nabla^2 z^+ + \nabla \cdot \hat{\mathbf{m}})^2 + \kappa_\theta \hat{\mathbf{m}}^2 + \kappa_{tw} (\nabla \times \hat{\mathbf{m}})^2 \\ &+ \frac{k_A}{b_0^2} \varepsilon^2 - \frac{\Omega}{b_0} (\nabla \cdot \hat{\mathbf{m}} + \nabla^2 z^+) \varepsilon, \end{aligned} \quad (20)$$

using the constants,

$$\begin{aligned} \Omega &\equiv 2k_c^\Sigma c_0 - 2\mu + k_A b_0, \\ k_c^b &\equiv k_c^\Sigma + \frac{1}{2} \Omega b_0 - \frac{1}{4} k_A b_0^2. \end{aligned} \quad (21)$$

Note that the splay terms, which are now written in terms of $\nabla^2 z^\pm$, $\nabla \cdot \hat{\mathbf{m}}$ and $\nabla \cdot \bar{\mathbf{m}}$, follow from Eq. (13) using the relationship $\nabla \cdot \mathbf{n}^{(\alpha)} = (-1)^{\alpha+1} \nabla^2 z^{(\alpha)} + \nabla \cdot \mathbf{m}^{(\alpha)}$ (Eqs. (3) and (4)).

What is the difference between k_c^Σ and k_c^b ? The bare bending modulus k_c^Σ reflects the cost of bending the membrane while holding the interfacial area per molecule $\Sigma^{(\alpha)}$ equal to Σ_0 . The bending modulus k_c^b reflects the cost of bending the membrane while holding the chain length $b^{(\alpha)}$ equal to b_0 .

Since both $\Sigma^{(\alpha)}$ and $b^{(\alpha)}$ fluctuate in general, a more useful parameter is the bending modulus k_c defined with respect to the neutral surface of each monolayer.⁶⁵ Using parallel surface arguments,⁶⁵ it can be shown that

$$k_c = k_c^b - \frac{\Omega^2}{4k_A}. \quad (22)$$

Within our model, k_c is also the coefficient of the q^{-4} term in the height fluctuation spectrum (see Sec. III). The distance d from $z^{(m)}$ to the neutral surface of each monolayer is given by

$$d = \frac{b_0}{2} + \frac{\Omega}{2k_A}. \quad (23)$$

Here, we have defined d such that $d=0$ and $d=b_0$ correspond to the neutral surface lying at $z^{(m)}$ and $z^{(\alpha)}$, respectively. Note

that in the limit $\Omega/k_A \ll b_0$, the neutral surface lies at the center of the monolayer and $k_c^b = k_c$. In Sec. V, we find d to be between $b_0/2$ and $3b_0/4$ for the systems we study.

Physically, the decoupling of the Hamiltonian into undulation and peristaltic contributions is analogous to finding the normal modes of a system of coupled springs. The peristaltic/undulation (symmetric/antisymmetric) decoupling of Eq. (18) was made possible by the fact that the opposing leaflets have identical material properties. Though an orthogonal decomposition would still be possible for non-identical monolayers, the resulting normal coordinates would contain the values of the material parameters. In general, the peristaltic/undulation decoupling is possible when the free energy expression for each monolayer is identical. This is true for our model since the free energy for each lipid is given by Eq. (12).

The total macroscopic free energy F contains energetic contributions originating from multiple degrees of freedom. Each monolayer free energy in Eq. (13) is a function of four independent scalar fields: $\{\Sigma^{(\alpha)}, \nabla \cdot \mathbf{n}^{(\alpha)}, \mathbf{m}^{(\alpha)}\}$. Since both monolayers are fused together at a common midplane, $z^{(m)}$, the bilayer free energy contains only seven independent scalar fields. Written in terms of $\{z^+, z^-, \varepsilon, \hat{\mathbf{m}}, \bar{\mathbf{m}}\}$, the Hamiltonian may be expressed as the sum of peristaltic and undulation modes.

F is parameterized by five elastic moduli $\{k_c, k_A, \Omega, \kappa_\theta, \kappa_{tw}\}$ and two “geometric” constants $\{b_0, c_0\}$ (k_c^Σ and k_c^b are combinations of these quantities [Eqs. (21) and (22)]). Though not used further in this work, the underlying theory derived in this section is general enough to account for finite chemical potential and non-periodic membrane geometries where Gaussian curvature may play a role, which would bring the moduli count to seven (add ζ and k_G). In Appendix A, we show how the macroscopic moduli are related to the molecular constants from the opposing forces model (Eq. (11)) $\{\gamma_s, B, \tau, \ell_c, l_h, v\}$ (the equilibrium quantities b_0 and Σ_0 are functions of these six parameters and are not independent variables).

The theory presented here relaxes various assumptions made in our previous work (BB). In addition to neglecting orientational effects, our previous treatment modeled each monolayer as a collection of rectangular lipids pointing purely in the z direction, such that the area per molecule measured at any surface would be equal to $\Sigma^{(\alpha)}$. As a result, the monolayer bending modulus was independent of its reference surface. In BB, it was also assumed that $\Sigma^{(1)} = \Sigma^{(2)}$ for simplicity. No such requirement is made here.

In summary, the macroscopic portion of the Hamiltonian we use for our analysis may be written as the sum (Eq. (18)) of peristaltic (Eq. (19)) and undulation (Eq. (20)) modes. With the exception of the contributions containing ε , various terms (or slight variations) from Eqs. (19) and (20) have appeared in previous derivations of the membrane deformation energy.^{14,21,22,27} In Fournier’s derivation,²⁷ an expression for the bilayer free energy is first written as a sum of all possible terms quadratic in $z^{(1)}$ and $z^{(2)}$ up to second derivatives and analogs of $\hat{\mathbf{m}}$ and $\bar{\mathbf{m}}$ up to first derivatives. Numerous terms are then discarded mainly due to symmetry arguments, while volume conservation is not enforced. While this method elegantly avoids any reliance on specific microscopic models,

it does not provide physical relationships between the coefficients of each term. For example, in contrast to the model presented in this paper, the coefficients of the $(\nabla^2 z^\pm)^2$, $(\nabla \cdot \hat{\mathbf{m}})^2$, and $(\nabla \cdot \hat{\mathbf{m}})^2$ terms are all distinct, resulting in a larger number of physical parameters. The method used here^{21,22} enforces the incompressibility constraint and provides a means to relate molecular parameters to macroscopic elastic moduli. By allowing for a bilayer of arbitrary shape, Eqs. (18)–(20) generalize the results from May and Ben-Shaul,^{21,22} which were calculated within a radially symmetric, undulation-free ($z^+ = z^{(m)} = \hat{\mathbf{m}} = 0$) geometry.

C. Protrusions

On length scales comparable to and smaller than the bilayer thickness, molecular structure becomes important. At this point, the macroscopic model (Eq. (18)), which treats the monolayer as an incompressible elastic continuum, begins to break down. The incompressibility condition (see Eq. (14) and Appendix A) was formulated in terms of continuum quantities: $dV^{(\alpha)}/dn^{(\alpha)} = v$, stating that the continuously defined lipid number density $dn^{(\alpha)}/dV^{(\alpha)}$ is constant everywhere within the membrane. This statement is not expected hold over length scales where the discrete nature of the lipids becomes important, where molecular number density becomes difficult to unambiguously assign and where the monolayer surfaces and director fields necessarily display roughness associated with the microscopic noise inherent to atomic scale motions. To account for these unavoidable deficiencies with the continuum elastic approach, we adopt a scheme similar to Lipowsky and Grothans,¹¹ where a continuum description of microscopic “protrusions” is introduced. Though this treatment is essentially phenomenological, we will show that the resulting expressions for the thermal averages are in excellent agreement with the simulation data.

We model protrusions as deviations from the average monolayer surfaces $z^{(\alpha)}$ along the corresponding normal vectors $\mathbb{N}^{(\alpha)}$ (see Fig. 1). Up to first order in $\{\mathbb{N}^{(\alpha)}, \lambda^{(\alpha)}/b_0\}$, the protrusions point purely in the z direction, with $\lambda^{(\alpha)} > 0$ corresponding to perturbing either monolayer interface upwards. The free energy density in the xy plane due to protrusions $f_\lambda^{(\alpha)}$ consists of a surface area term, reflecting the interfacial tension, plus a binding term to keep the fluctuations localized to the coarse-grained fields $z^{(\alpha)}$ (BB):

$$f_\lambda^{(\alpha)} = \gamma_\lambda \Delta A^{(\alpha)} + \frac{k_\lambda}{2} [\lambda^{(\alpha)}]^2,$$

where the surface area difference introduced by the fields $\lambda^{(\alpha)}$ is

$$\Delta A^{(\alpha)} = \frac{1}{2} [(\nabla(z^{(\alpha)} + \lambda^{(\alpha)}))^2 - (\nabla z^{(\alpha)})^2]. \quad (24)$$

The area of the sheets $z^{(\alpha)}$ is subtracted off because the interfacial energy associated with molecularly smooth shape changes is already incorporated within $f_{\text{plane}}^{(\alpha)}$. We consider $b^{(\alpha)}$ to be unaffected by protrusions because volume is not conserved on a molecular level. Microscopic changes in the hydrocarbon chain length may be taken into account by the k_λ term in Eq. (25).

The total contribution of the protrusion energetics is the sum from both monolayers: $f_\lambda = f_\lambda^{(1)} + f_\lambda^{(2)}$. In terms of the symmetric/antisymmetric variables in Eqs. (1) and (7), the total free energy due to protrusions is

$$f_\lambda = \gamma_\lambda [(\nabla \lambda^+)^2 + (\nabla \lambda^-)^2 + 2\nabla z^+ \cdot \nabla \lambda^+ + 2\nabla z^- \cdot \nabla \lambda^-] + k_\lambda [(\lambda^+)^2 + (\lambda^-)^2]. \quad (25)$$

The total free energy density for the membrane is $f_{\text{plane}}^{(1)} + f_{\text{plane}}^{(2)} + f_\lambda$. Writing the total bilayer free energy in terms of undulation and peristaltic modes,

$$\mathcal{F} = \int (f_p(z^-, \hat{\mathbf{m}}, \lambda^-) + f_u(z^+, \hat{\mathbf{m}}, \varepsilon, \lambda^+)) \mathbf{dr}, \quad (26)$$

$$\begin{aligned} f_p(z^-, \hat{\mathbf{m}}, \lambda^-) &= \frac{k_A}{b_0^2} (z^-)^2 + k_c^b (\nabla^2 z^- + \nabla \cdot \hat{\mathbf{m}})^2 \\ &+ 2k_c^\Sigma c_0 (\nabla \cdot \hat{\mathbf{m}} + \nabla^2 z^-) + \frac{\Omega}{b_0} (\nabla \cdot \hat{\mathbf{m}} + \nabla^2 z^-) z^- \\ &+ \kappa_\theta \hat{\mathbf{m}}^2 \kappa_{\text{tw}} (\nabla \times \hat{\mathbf{m}})^2 \\ &+ \gamma_\lambda (\nabla \lambda^-)^2 + 2\gamma_\lambda \nabla z^- \cdot \nabla \lambda^- + k_\lambda (\lambda^-)^2, \end{aligned} \quad (27)$$

$$\begin{aligned} f_u(z^+, \hat{\mathbf{m}}, \varepsilon, \lambda^+) &= k_c^b (\nabla^2 z^+ + \nabla \cdot \hat{\mathbf{m}})^2 + \kappa_\theta \hat{\mathbf{m}}^2 \\ &+ \kappa_{\text{tw}} (\nabla \times \hat{\mathbf{m}})^2 + \frac{k_A}{b_0^2} \varepsilon^2 - \frac{\Omega}{b_0} (\nabla \cdot \hat{\mathbf{m}} + \nabla^2 z^+) \varepsilon \\ &+ \gamma_\lambda (\nabla \lambda^+)^2 + 2\gamma_\lambda \nabla z^+ \cdot \nabla \lambda^+ + k_\lambda (\lambda^+)^2. \end{aligned} \quad (28)$$

These Eqs. (26)–(28) summarize the primary theoretical results of this paper. The fluctuation spectra discussed in Sec. III follow immediately from these expressions.

By including the protrusion contribution f_λ to the total free energy, we have introduced two additional scalar fields $\{\lambda^+, \lambda^-\}$ and two elastic parameters $\{\gamma_\lambda, k_\lambda\}$. Though we assume that two elastic parameters are needed to model protrusions in general, we show in Sec. V that γ_λ may be approximated as zero for the systems we have analyzed.

III. FLUCTUATION SPECTRA OF HOMOGENEOUS MEMBRANES

The free energy of the bilayer determines the nature of its thermal fluctuations as a function of wave number \mathbf{q} . Measurement of the height fluctuations $\langle |h_{\mathbf{q}}|^2 \rangle$ via simulation has become a standard method^{29,39–54} to calculate the bending rigidity of homogeneous fluid membranes. Analysis of thickness fluctuations $\langle |t_{\mathbf{q}}|^2 \rangle$ has also been conducted^{29,41–44,50,51} in order to extract the value of k_A .

In MNK, tilt fluctuations were analyzed within the context of the Hamm and Kozlov¹⁴ model. However, their treatment was simplified since the Hamm and Kozlov theory only pertains to non-stretched monolayers in the incompressible continuum limit. MNK reported that membrane fluctuations may be adequately described by the macroscopic Hamm and Kozlov model down to length scales approaching the interlipid distance. By analyzing the spectra of many previously unmeasured quantities, we will show that a microscopic formulation of protrusions is required to accurately describe the tilt fluctuation spectra at length scales comparable to the bilayer thickness.

In this subsection, we derive exact forms for the height, thickness, and tilt fluctuations predicted by Eqs. (26)–(28), respectively. The tilt fluctuations, which involve vector quantities, are analyzed in terms of longitudinal and transverse components relative to \mathbf{q} . The resulting decomposition will further illuminate the role of both twist and protrusions. The predicted spectra agree very well with the simulation data. Fitting the exact expressions allows us to determine the values of the elastic constants.

For a homogeneous membrane in a square box of area L^2 and periodic boundary conditions, the Hamiltonian may be written in Fourier space using Eqs. (26)–(28). We use the Fourier transform pair,

$$\begin{aligned} \mathbf{g}_{\mathbf{q}} &= \frac{1}{L} \int \mathbf{g}(\mathbf{r}) e^{-i\mathbf{q}\cdot\mathbf{r}} d\mathbf{r}, \\ \mathbf{g}(\mathbf{r}) &= \frac{1}{L} \sum_{\mathbf{q}} \mathbf{g}_{\mathbf{q}} e^{i\mathbf{q}\cdot\mathbf{r}}, \end{aligned} \quad (29)$$

for an arbitrary scalar function $\mathbf{g}(\mathbf{r})$. When $\mathbf{g}(\mathbf{r})$ is real, which is the case for all quantities we discuss, $\mathbf{g}_{\mathbf{q}}^* = \mathbf{g}_{-\mathbf{q}}$. The values of the wave number are given by $\mathbf{q} = 2\pi(n, m)/L$ for the integers $n, m = \{-M/2, \dots, 0, \dots, M/2 - 1\}$, where M is dictated by a short wavelength cutoff.

In Fourier space, the vector quantities $\hat{\mathbf{m}}$, $\bar{\mathbf{m}}$, and $\nabla\lambda^{\pm}$ may be decomposed in the following way. Any two-dimensional vector \mathbf{c} may be written in terms of its longitudinal and transverse components,

$$c_{\mathbf{q}}^{\parallel} = \frac{\mathbf{q} \cdot \mathbf{c}_{\mathbf{q}}}{q}, \quad c_{\mathbf{q}}^{\perp} = \frac{(\mathbf{q} \times \mathbf{c}_{\mathbf{q}}) \cdot \hat{\mathbf{z}}}{q}. \quad (30)$$

Note that $c_{\mathbf{q}}^{\perp*} = -c_{-\mathbf{q}}^{\perp}$ and $c_{\mathbf{q}}^{\parallel*} = -c_{-\mathbf{q}}^{\parallel}$ when $\mathbf{c}(\mathbf{r})$ is real. Within this basis, the differential operators in Eqs. (27) and (28) appear particularly simple in Fourier space and the longitudinal and transverse components of the Hamiltonian are decoupled: $\nabla \times \mathbf{c} \rightarrow iq c_{\mathbf{q}}^{\perp} \hat{\mathbf{z}}$, $\nabla \cdot \mathbf{c} \rightarrow iq c_{\mathbf{q}}^{\parallel}$ and $\nabla\lambda^{\pm} \rightarrow i\mathbf{q}\lambda_{\mathbf{q}}^{\pm}$. In Fourier space, integration over real space

is replaced by a sum over modes:

$$\begin{aligned} \mathcal{F}_u &= \sum_{\mathbf{q}} \left\{ k_c^b q^4 |z_{\mathbf{q}}^+|^2 + \frac{k_A}{b_0^2} |\varepsilon_{\mathbf{q}}|^2 + (k_{\lambda} + \kappa_{\theta} q^2) |\lambda_{\mathbf{q}}^+|^2 \right. \\ &\quad + (\kappa_{\theta} + k_c^b q^2) |\hat{m}_{\mathbf{q}}^{\parallel}|^2 + (\kappa_{\theta} + \kappa_{tw} q^2) |\hat{m}_{\mathbf{q}}^{\perp}|^2 \\ &\quad + \frac{q^2 \Omega}{b_0} \text{Re}[z_{\mathbf{q}}^+ \varepsilon_{-\mathbf{q}}] + 2q \text{Im}[k_c^b q^2 \hat{m}_{\mathbf{q}}^{\parallel} z_{-\mathbf{q}}^+ + \frac{\Omega}{2b_0} \hat{m}_{\mathbf{q}}^{\parallel} \varepsilon_{-\mathbf{q}} \\ &\quad \left. + \kappa_{\theta} \lambda_{\mathbf{q}}^+ \hat{m}_{-\mathbf{q}}^{\parallel}] + 2q^2 \gamma_{\lambda} \text{Re}[z_{\mathbf{q}}^+ \lambda_{-\mathbf{q}}^+] \right\}, \end{aligned} \quad (31)$$

$$\begin{aligned} \mathcal{F}_p &= \sum_{\mathbf{q}} \left\{ \left(\frac{k_A}{b_0^2} - \frac{q^2 \Omega}{b_0} + k_c^b q^4 \right) |z_{\mathbf{q}}^-|^2 + (k_{\lambda} + \kappa_{\theta} q^2) |\lambda_{\mathbf{q}}^-|^2 \right. \\ &\quad + (\kappa_{\theta} + k_c^b q^2) |\bar{m}_{\mathbf{q}}^{\parallel}|^2 + (\kappa_{\theta} + \kappa_{tw} q^2) |\bar{m}_{\mathbf{q}}^{\perp}|^2 \\ &\quad \left. + 2q \text{Im} \left[\left(k_c^b q^2 - \frac{\Omega}{2b_0} \right) \bar{m}_{\mathbf{q}}^{\parallel} z_{-\mathbf{q}}^- \right] + 2q^2 \gamma_{\lambda} \text{Re}[z_{\mathbf{q}}^- \lambda_{-\mathbf{q}}^-] \right\}, \end{aligned} \quad (32)$$

where \mathcal{F}_u and \mathcal{F}_p are the undulation and peristaltic portions of the total free energy, respectively.

In order to calculate thermal averages, it is convenient to express the above equations in terms of matrices. Defining the vectors

$$\begin{aligned} \mathbf{f}_u(\mathbf{q}) &= (z_{\mathbf{q}}^+, \hat{m}_{\mathbf{q}}^{\parallel}, \lambda_{\mathbf{q}}^+, \hat{m}_{\mathbf{q}}^{\perp}, \varepsilon_{\mathbf{q}}), \\ \mathbf{f}_p(\mathbf{q}) &= (z_{\mathbf{q}}^-, \bar{m}_{\mathbf{q}}^{\parallel}, \lambda_{\mathbf{q}}^-, \bar{m}_{\mathbf{q}}^{\perp}), \end{aligned} \quad (33)$$

the two contributions may be written as

$$\begin{aligned} \mathcal{F}_u &= \sum_{\mathbf{q}} \mathbf{f}_u(-\mathbf{q}) \otimes \mathbf{A} \otimes \mathbf{f}_u^T(\mathbf{q}), \\ \mathcal{F}_p &= \sum_{\mathbf{q}} \mathbf{f}_p(-\mathbf{q}) \otimes \mathbf{B} \otimes \mathbf{f}_p^T(\mathbf{q}), \end{aligned} \quad (34)$$

where “ \otimes ” denotes matrix multiplication. The matrices \mathbf{A} and \mathbf{B} are given by

$$\mathbf{A} = \begin{pmatrix} k_c^b q^4 & -ik_c^b q^3 & \gamma_{\lambda} q^2 & 0 & q^2 \Omega / 2b_0 \\ ik_c^b q^3 & \kappa_{\theta} + k_c^b q^2 & 0 & 0 & iq \Omega / 2b_0 \\ \gamma_{\lambda} q^2 & 0 & k_{\lambda} + \gamma_{\lambda} q^2 & 0 & 0 \\ 0 & 0 & 0 & \kappa_{\theta} + \kappa_{tw} q^2 & 0 \\ q^2 \Omega / 2b_0 & -iq \Omega / 2b_0 & 0 & 0 & k_A / b_0^2 \end{pmatrix}, \quad (35)$$

$$\mathbf{B} = \begin{pmatrix} \frac{k_A}{b_0^2} - \frac{q^2 \Omega}{b_0} + k_c^b q^4 & \frac{iq \Omega}{2b_0} - ik_c^b q^3 & \gamma_{\lambda} q^2 & 0 & 0 \\ -\frac{iq \Omega}{2b_0} + ik_c^b q^3 & \kappa_{\theta} + k_c^b q^2 & 0 & 0 & 0 \\ \gamma_{\lambda} q^2 & 0 & k_{\lambda} + \gamma_{\lambda} q^2 & 0 & 0 \\ 0 & 0 & 0 & 0 & \kappa_{\theta} + \kappa_{tw} q^2 \end{pmatrix}. \quad (36)$$

Note that since

$$\int_{L^2} \nabla^2 z^- \, d\mathbf{r} = \int_{L^2} (\nabla \cdot \bar{\mathbf{m}}) \, d\mathbf{r} = 0$$

under periodic boundary conditions, two terms from Eq. (27) do not appear in the Fourier representation. Consequently, one cannot measure c_0 directly, but only the constant Ω/b_0 . To measure c_0 independently, the membrane stress profile will be used (see Sec. V).

Within our formalism the thermal fluctuations of several previously unmeasured quantities may be calculated. In general, when the free energy,

$$\mathcal{H} = \frac{1}{2} \sum_{\mathbf{q}} \mathbf{f}(-\mathbf{q}) \otimes \mathbf{D} \otimes \mathbf{f}^T(\mathbf{q})$$

can be written in terms of a Hermitian matrix \mathbf{D} , the fluctuations satisfy^{52,65,66}

$$\langle \mathbf{f}^T(\mathbf{q}) \otimes \mathbf{f}(\mathbf{q}') \rangle = k_B T \delta_{\mathbf{q},-\mathbf{q}'} \mathbf{D}^{-1},$$

which is simply a statement of the equipartition of energy for the Fourier components of real-valued physical quantities. The full expressions for the thermal averages are given in Appendix D. Most of the expressions are complicated. The only simple ones are those of $\langle |\hat{p}_{\mathbf{q}}^{\perp}|^2 \rangle$ and $\langle |\bar{p}_{\mathbf{q}}^{\perp}|^2 \rangle$:

$$\langle |\hat{p}_{\mathbf{q}}^{\perp}|^2 \rangle = \langle |\bar{p}_{\mathbf{q}}^{\perp}|^2 \rangle = \frac{k_B T}{2(\kappa_{\theta} + \kappa_{\text{tw}} q^2)}.$$

These quantities decrease on small length scales (increasing q) due to the energetic cost of twist. Since the transverse contributions are decoupled from the rest of the Hamiltonian in Eqs. (35) and (36), their thermal averages may be obtained by inverting the corresponding matrix elements. Protrusions only affect the measured tilt parallel to \mathbf{q} (through $\nabla \lambda^{(\omega)}$) and are therefore absent in $\langle |\hat{p}_{\mathbf{q}}^{\perp}|^2 \rangle$ and $\langle |\bar{p}_{\mathbf{q}}^{\perp}|^2 \rangle$.

In the limit ($\kappa_{\theta} \rightarrow \infty$) the expressions for $\langle |h_{\mathbf{q}}|^2 \rangle$ and $\langle |t_{\mathbf{q}}|^2 \rangle$ reduce to those given in BB, in which the lipids

were implicitly assumed to be normal to the interfaces (note slight changes in notation). Additional limiting cases are discussed in Sec. III B. For systems where the coupling between protrusions and the monolayer surfaces is weak, the general expressions may be greatly simplified (BB). It is well established^{29,39–50,52–54} that the long wavelength height fluctuations of a nearly flat bilayer at zero surface tension follow

$$\langle |h_{\mathbf{q}}|^2 \rangle = \frac{k_B T}{2K_c q^4}, \quad (37)$$

where K_c is an effective bending rigidity. Expanding Eq. (D1) around small q ,

$$\langle |h_{\mathbf{q}}|^2 \rangle = \frac{k_B T}{2(k_c - \gamma_{\lambda}^2/k_{\lambda}) q^4} + O\left(\frac{1}{q^2}\right),$$

the form in Eq. (37) is recovered, but with a renormalized bending modulus:

$$K_c = k_c(1 - \gamma_{\lambda}^2/k_c k_{\lambda}). \quad (38)$$

As derived by Lipowsky and Grotehans,¹¹ Eq. (38) shows that protrusions effectively soften the membrane bending modes. Note that K_c remains positive only when $\gamma_{\lambda}^2/k_c k_{\lambda} < 1$, which sets limitations on the relative magnitudes of the elastic constants. The quantity $\gamma_{\lambda}^2/k_c k_{\lambda}$ represents the coupling strength between protrusions and bending modes. In Sec. V, we find that this quantity is sufficiently small to be neglected for the systems we study.

A. Decoupled protrusion/bending approximation

The coupling between protrusions and bending may be effectively turned off by setting the $z_{\mathbf{q}}^+ \lambda_{-\mathbf{q}}^+$ and $z_{\mathbf{q}}^- \lambda_{-\mathbf{q}}^-$ terms in Eqs. (31) and (32) equal to zero. The spectra then become

$$\langle |h_{\mathbf{q}}|^2 \rangle = \frac{k_B T}{2} \left(\frac{1}{k_c q^4} + \frac{1}{\kappa_{\theta} q^2} + \frac{1}{(k_{\lambda} + \gamma_{\lambda} q^2)} \right), \quad (39)$$

$$\langle |\hat{p}_{\mathbf{q}}^{\parallel}|^2 \rangle = \frac{k_B T}{2} \left(\frac{1}{\kappa_{\theta}} + \frac{q^2}{(k_{\lambda} + \gamma_{\lambda} q^2)} \right), \quad (40)$$

$$\langle |t_{\mathbf{q}}|^2 \rangle = \frac{k_B T}{2} \left(\frac{4(k_c^b q^2 + \kappa_{\theta})}{4k_c^b \kappa_{\theta} q^4 - \frac{\Omega}{b_0} \left(\frac{\Omega}{b_0} + 4\kappa_{\theta} \right) q^2 + 4\frac{k_A}{b_0^2} (k_c^b q^2 + \kappa_{\theta})} + \frac{1}{(k_{\lambda} + \gamma_{\lambda} q^2)} \right), \quad (41)$$

$$\langle |\bar{p}_{\mathbf{q}}^{\parallel}|^2 \rangle = \frac{k_B T}{2} \left(\frac{4 \left(k_c^b q^4 - \frac{\Omega q^2}{b_0} + \frac{k_A}{b_0^2} \right)}{4\kappa_{\theta} k_c^b q^4 - \frac{\Omega}{b_0} \left(\frac{\Omega}{b_0} + 4\kappa_{\theta} \right) q^2 + 4\frac{k_A}{b_0^2} (k_c^b q^2 + \kappa_{\theta})} + \frac{q^2}{(k_{\lambda} + \gamma_{\lambda} q^2)} \right), \quad (42)$$

$$\langle |\hat{p}_{\mathbf{q}}^{\perp}|^2 \rangle = \langle |\bar{p}_{\mathbf{q}}^{\perp}|^2 \rangle = \frac{k_B T}{2(\kappa_{\theta} + \kappa_{\text{tw}} q^2)}. \quad (43)$$

Since the protrusion contributions are decoupled from the rest of the free energy, the variances simply add and the expressions become more susceptible to physical interpretation. The expressions for height and thickness contain the protrusion contribution,

$$\langle |\lambda_{\mathbf{q}}^{\pm}|^2 \rangle = \frac{k_B T}{2(k_{\lambda} + \gamma_{\lambda} q^2)}.$$

Just as with the coupled expressions, Eqs. (39) and (41) reduce to the decoupled result in BB for $\kappa_{\theta} \rightarrow \infty$.

The expression for $\langle |h_{\mathbf{q}}|^2 \rangle$ exhibits the well-known $\propto q^{-4}$ behavior at low wave numbers. The second term in Eq. (39) reflects the contribution of molecular tilt by means of the κ_{θ} term in Eq. (28). After extracting the values of the elastic constants from the simulation data, we found that the value of this term was greater than or comparable to the q^{-4} term at all but the lowest simulated wave numbers. Excluding the protrusion term, Eq. (39) has been derived previously (MNK).

Physically, the divergent behavior of $\langle |h_{\mathbf{q}}|^2 \rangle$ as $q \rightarrow 0$ reflects the fact that low curvature (long wavelength) deformations cost less energy than shorter wavelength deformations (Eq. (20)). The amplitude of height fluctuations, therefore, grows with system size. Since the deformation energy of a free membrane is a function of derivatives in height, and not the height itself, the point at $q = 0$ is not relevant. However, this is not the case for the other averages in Eqs. (40)–(43). Neglecting protrusions, the values of $\langle |t_{\mathbf{q}}|^2 \rangle$, $\langle |\bar{p}_{\mathbf{q}}^{\parallel}|^2 \rangle$, $\langle |\hat{p}_{\mathbf{q}}^{\perp}|^2 \rangle$, $\langle |\bar{p}_{\mathbf{q}}^{\perp}|^2 \rangle$, and $\langle |\bar{p}_{\mathbf{q}}^{\pm}|^2 \rangle$ at $q = 0$ are determined by their corresponding moduli: k_A for thickness, and κ_{θ} for tilt.

The separate contributions of macroscopic tilt and protrusions are easily identified for Eqs. (40)–(42) as well. While fluctuations in measured tilt are constant at long wavelengths, the effect of protrusions becomes increasingly important at small length scales. Since the measured tilt is a function of gradients in the protrusion field (Eq. (10)), their contributions to $\langle |\hat{p}_{\mathbf{q}}^{\parallel}|^2 \rangle$ and $\langle |\bar{p}_{\mathbf{q}}^{\parallel}|^2 \rangle$ are simply $q^2 \langle |\lambda_{\mathbf{q}}^{\pm}|^2 \rangle$, causing the tilt averages to grow with q . If protrusions were not present, $\langle |\hat{p}_{\mathbf{q}}^{\parallel}|^2 \rangle$ and $\langle |\bar{p}_{\mathbf{q}}^{\parallel}|^2 \rangle$ would level out to $k_B T / 2\kappa_{\theta}$.

Aside from the protrusion contribution, $\langle |\hat{p}_{\mathbf{q}}^{\parallel}|^2 \rangle$ is the only average which is constant. This can be understood by examining the undulation portion of the macroscopic free energy (Eq. (20)). Making the substitution $\mathbf{w} = \nabla^2 z^+ + \nabla \cdot \hat{\mathbf{m}}$, we see that $\hat{\mathbf{m}}$ becomes completely decoupled from the rest of the Hamiltonian,

$$\mathcal{F}_{\text{macro}}^{\hat{\mathbf{m}}} = \sum_{\mathbf{q}} \kappa_{\theta} |\hat{m}_{\mathbf{q}}^{\parallel}|^2 + (\kappa_{\theta} + q^2 \kappa_{\text{tw}}) |\hat{m}_{\mathbf{q}}^{\perp}|^2. \quad (44)$$

The contribution parallel to \mathbf{q} is independent of wave number so that the corresponding macroscopic tilt average is given by $\langle |\hat{m}_{\mathbf{q}}^{\parallel}|^2 \rangle = k_B T / 2\kappa_{\theta}$.

Even in the decoupled protrusion/bending approximation, the expressions for $\langle |t_{\mathbf{q}}|^2 \rangle$ and $\langle |\bar{p}_{\mathbf{q}}^{\parallel}|^2 \rangle$ are still cumbersome. This is due to the fact that peristaltic modes are out of phase deformations in which multiple competing forces are involved. At long wavelengths $\langle |t_{\mathbf{q}}|^2 \rangle \rightarrow k_B T (b_0^2 / 2k_A + 1/2k_{\lambda})$, reflecting the energetic cost of pure stretching/compression. In the simulation section we find that $k_{\lambda} \gg k_A / b_0^2$, so that $\langle |t_{\mathbf{q}}|^2 \rangle \propto 1/k_A$ for $q \rightarrow 0$.

As shown in Figs. 9 and 10, both $\langle |t_{\mathbf{q}}|^2 \rangle$ and $\langle |\bar{p}_{\mathbf{q}}^{\parallel}|^2 \rangle$ behave non-monotonically for the cases of the two bilayers we simulated. The non-monotonicity in the thickness fluctuations may be understood in terms of the peristaltic portion of the macroscopic free energy (Eq. (19)) in the absence of symmetric tilt,

$$\begin{aligned} f_p(z^-, \hat{\mathbf{m}} = 0) \\ = \frac{k_A}{b_0^2} (z^-)^2 + k_c^b (\nabla^2 z^-)^2 + 2k_c^{\Sigma} c_0 \nabla^2 z^- + \frac{\Omega}{b_0} z^- \nabla^2 z^-. \end{aligned}$$

For periodic boundaries, the linear term containing c_0 will not contribute to the free energy. Assume that the deviation in thickness is given by a single wave: $z^- = \beta \cos(\mathbf{q} \cdot \mathbf{r})$. If $\Omega > 0$ the cross term will have a negative value, so that a certain intermediate wave number ($0 < q < \infty$) will yield the lowest free energy value. For both of the membrane systems we analyzed, we found $\Omega > 0$, explaining the peak in $\langle |t_{\mathbf{q}}|^2 \rangle$ in Figs. 9 and 10. A similar argument can be made to explain the dip in $\langle |\bar{p}_{\mathbf{q}}^{\parallel}|^2 \rangle$.

In the long wavelength limit, all four tilt averages are equal to $k_B T / 2\kappa_{\theta}$, corresponding to pure tilt deformations. In this limit, our expressions reduce to the value derived in MNK, in which a constant value was predicted over all wavelengths. At short wavelengths both $\langle |\bar{p}_{\mathbf{q}}^{\parallel}|^2 \rangle$ and $\langle |\hat{p}_{\mathbf{q}}^{\parallel}|^2 \rangle$ are larger than their $q = 0$ values due to the amplifying effect of protrusions. In the regime $k_A \rightarrow \infty$, $k_{\lambda} \rightarrow \infty$, and $\kappa_{\text{tw}} \rightarrow 0$, $\bar{p}_{\mathbf{q}}^{\parallel}$ is decoupled from the thickness, and the four tilt averages would be equal to the result from MNK. By including the effects of protrusions, peristaltic modes and twist, we will show that our model reproduces the correct wavelength dependence of the tilt spectra measured in our simulations.

B. $\gamma_{\lambda} = 0$ approximation

For certain systems, it is possible to make the further approximation that the protrusion contribution to the free energy is purely due to Gaussian white noise. By neglecting the microscopic surface tension ($\gamma_{\lambda} = 0$), Eq. (25) then becomes

$$f_{\lambda} = k_{\lambda} [(\lambda^+)^2 + (\lambda^-)^2].$$

In this case the coupling between bending and protrusion modes is not just weak, but entirely non-existent. In Sec. V, we find that Eqs. (39)–(43) with $\gamma_{\lambda} = 0$ fit the data very well. In other words, invoking a microscopic surface tension is unnecessary in order to explain the simulation data, as long as the tilt degree of freedom is taken into account.

IV. SIMULATION DETAILS

A. Implicit solvent model

A previously developed implicit solvent coarse-grained lipid model⁴⁵ (CG) (Figs. 5 and 7) was implemented within LAMMPS.⁶⁷ A few minor modifications to the original model had to be made to make this implementation possible. The original rigid bonds were replaced by stiff harmonic bonds

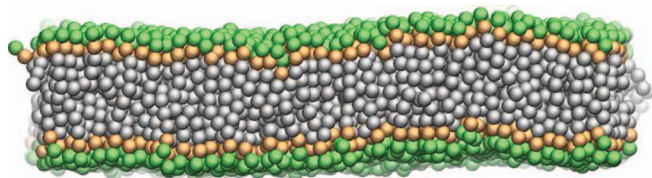


FIG. 5. Snapshot from our implicit solvent model (CG). Each lipid consists of five beads (see Fig. 7).

$U_b(r) = k_b(r - \sigma)^2$, with $k_b = 5 \times 10^3 \epsilon/\sigma^2$ (see Goetz and Lipowsky⁶⁸ for a rationale). Another difference with the original model is the truncation scheme for all non-bonded potentials (U_{core} , U_{tail} , and U_{int}): here we used the same cutoffs as in Brannigan, Philips, and Brown,⁴⁵ but employ a third-order polynomial force switching function⁶⁹ with a switching region of 0.5 Å. All pairwise potentials were tabulated on a dense equidistant radial mesh, with a mesh spacing of 0.01 Å, and linear interpolation was used to calculate the energy and forces. The pairwise neighbor list was created by binning⁶⁷ along with a “skin” distance of 1.5σ and updated every time step after a delay of 10 steps after the previous build, but only if a bead has moved more than half the skin distance.

Dynamics trajectories were generated within the isobaric zero pressure ensemble corresponding to a zero surface tension simulation⁷⁰ for a square bilayer patch composed of $N = 3200$ lipids and $L \approx 30$ nm (Fig. 5) in an orthorhombic simulation box. The initial geometry was constructed by placing the lipids laterally on a equidistant 40×40 square mesh with grid spacing of σ in each dimension, followed by equilibration. The time scale of the present model was chosen as $\tau = (m\sigma^2/\epsilon)^{1/2} \simeq 3$ ps, with all beads having the same mass m . Temperature was controlled via a Langevin thermostat with damping parameter of 0.12 ps; as in BB, all simulations were performed at $T = 0.85\epsilon$. To maintain the tensionless state of the bilayer, a Nosé-Hoover barostat with damping parameter of 1 ps was used to control the lateral pressure tensor components P_{xx} and P_{yy} at a zero target pressure, preserving the square shape of the simulation box while the box size in z direction was kept fixed. The equations of motion were integrated with a time step of $\delta t = 0.002\tau$, and system coordinates, or “frames,” were saved every 2×10^4 time steps for analysis.

The stress profile across the bilayer (Fig. 6), which is given by the difference between the normal and lateral pressures,

$$s(z) = P_{zz}(z) - \frac{1}{2}[P_{xx}(z) + P_{yy}(z)] \quad (45)$$

was calculated according to the scheme in Lindahl and Edholm.⁷² We used an off-the-shelf implementation of this algorithm from the NAMD molecular dynamics simulator.⁷³ A trajectory was first generated for a bilayer of 128 lipids, removing possible center-of-mass drift. Then, the trajectory was post-processed using NAMD, dividing the simulation box along $\hat{e}_z = (0, 0, 1)$, with $L_z = 20\sigma$, into 100 slabs of equal thickness. Within the NAMD pressure analysis package, the Harasima⁷⁴ convention was used for calculating the stress profile.

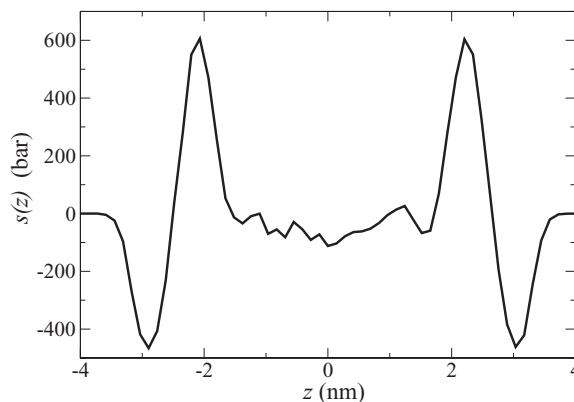


FIG. 6. The stress profile within the bilayer for our implicit solvent model (CG). The troughs at ± 3 nm represent the repulsion between the head beads, while the peaks at ± 2 nm are due to the strong attraction between interface beads.⁷¹ The monolayer spontaneous curvature c_0 is related to $s(z)$ through Eq. (47). The stress profile we measured for the MARTINI model of DPPC is the same as in the original paper.⁵⁵

B. MARTINI force field model (DPPC)

We also simulated the coarse-grained MARTINI model^{55,56} for DPPC and explicit water. As shown in Fig. 7, each lipid is modeled with 12 beads. The simulations were run within the GROMACS package.^{75–77} The temperature and pressure were maintained at 325 K and 1 bar using the Berendsen coupling scheme (Fig. 7). A vanishing surface tension was maintained semi-isotropically, in which the pressure coupling is isotropic in the x and y directions, but

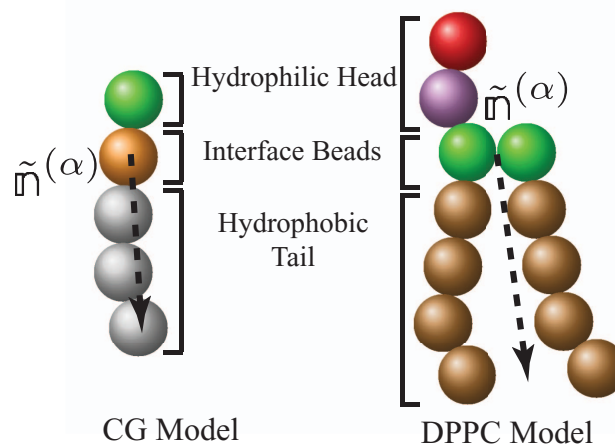


FIG. 7. A schematic diagram of the force fields used in the two lipid systems we studied. We also illustrate how the director $\tilde{\mathbf{m}}^{(\alpha)}$ is measured within each model. Note that for visual purposes $\tilde{\mathbf{m}}^{(\alpha)}$ is not normalized. Left: Our implicit solvent model (CG). Each lipid consists of a hydrophilic head bead (green), an interfacial bead (orange), and three hydrophobic tail beads (gray). Though the potentials were designed to mimic generic intermolecular forces, no explicit electrostatic interactions are present. $\tilde{\mathbf{m}}^{(\alpha)}$ points from the interfacial bead toward the last tail bead. Right: For the MARTINI force field (DPPC), each lipid consists of a positively charged bead representing the choline group (red), a negatively charged bead representing the phosphate group (purple), two beads of intermediate hydrophobicity representing the glycerol ester linkage (green), and two chains of four hydrophobic beads each, representing the hydrocarbons (brown). The charged beads interact via a shifted Coulombic potential energy function.⁵⁵ $\tilde{\mathbf{m}}^{(\alpha)}$ points from the midpoint of the interfacial beads toward the midpoint of the last tail beads.

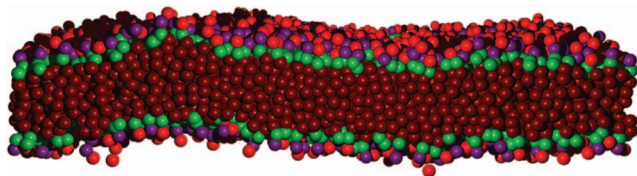


FIG. 8. Snapshot from the MARTINI force field model of DPPC. Each lipid consists of 12 beads (see Fig. 7). Solvent particles are not shown.

adjusted independently in z . Periodic boundary conditions were used in all directions.

A self-assembled bilayer patch with 128 lipids was obtained from the MARTINI-related web resource.⁷⁸ The size of the patch was then increased by a factor of two in the lateral directions by replicating the membrane. The equations of motion were integrated with a time step of $\delta t = 0.04$ ps. After an equilibration time of 500 ns, the replication process was repeated again with an additional equilibration time of 1 μ s. This resulted in a system with $N = 2048$ lipids spanning a square $L \approx 25$ nm in width, surrounded by 32000 water beads (Fig. 8). A production run of 2.4 μ s was simulated, over which the system coordinates were saved for analysis every 25000 steps.

The stress profile was measured for the 128 lipid system using an add-on to the GROMACS package,⁷⁹ which uses the technique described in Lindahl and Edholm⁷² along with the Irving-Kirkwood⁸⁰ convention of contour choice. Though the stress profile calculation for CG employs the Harasima⁷⁴ convention, it has been shown that the contour choices of both Irving-Kirkwood and Harasima yield consistent results for planar bilayers.⁸¹

V. COMPARISON TO THEORY

As described in Appendix C, the thermal fluctuations were analyzed by mapping the positions and orientations of the molecules onto a square $M \times M$ lattice. The location of the polar/non-polar interface on each lipid, or “interface point,” was chosen according to the force-field scheme of each simulation. For CG, the interface point was the location of the interface bead. For DPPC, the midpoint between the two beads of intermediate hydrophobicity was used. In order to measure the tilt of a given molecule, a director pointing from the interface point along its length had to be defined as well.

The director of each molecule was assigned by drawing a normalized vector pointing from the interface point to a “tail point,” which represents the end of the molecule (Fig. 7). The choice of this location for CG was that of the fifth bead. Unlike CG, more choices are available for the DPPC lipids. We chose the midpoint between the beads at the end of each hydrocarbon chain. The exact choice of the tail point and its effect on the tilt spectra were explored in MNK. It was shown that the tilt spectra have nearly the same shape as a function of q , but are shifted by a relative magnitude of less than 10%.

For each simulation, six data sets were collected in our fitting procedure:

$$S = \{ \langle |h_{\mathbf{q}}|^2 \rangle, \langle |t_{\mathbf{q}}|^2 \rangle, \langle |\hat{p}_{\mathbf{q}}^\perp|^2 \rangle, \langle |\bar{p}_{\mathbf{q}}^\perp|^2 \rangle, \langle |\hat{p}_{\mathbf{q}}^\parallel|^2 \rangle, \langle |\bar{p}_{\mathbf{q}}^\parallel|^2 \rangle \}.$$

We first obtained values for κ_θ and κ_{tw} by fitting the spectra for $\langle |\hat{p}_{\mathbf{q}}^\perp|^2 \rangle$ and $\langle |\bar{p}_{\mathbf{q}}^\perp|^2 \rangle$ to Eq. (43). We then fit the remaining data sets to Eqs. (39)–(43) with $\gamma_\lambda = 0$ using $\{k_c, k_A/b_0^2, \Omega/b_0, k_\lambda\}$ as free parameters. In contrast to BB, all spectra were fit on linear, rather than logarithmic scales so that the small tilt averages were not highly weighted. Due to the equal lattice spacing in the data as a function of \mathbf{q} , there exist more data points at higher wave numbers when the measured spectra are plotted as a function of q . As a result, we found that the fits were biased towards the high q data, giving rise to a lower value of k_A than the low q data would predict. We therefore used only data points located on the q_x and q_y axes.

Our curve-fitting algorithm is similar to BB, but with up to four simultaneous fits instead of two. The sum of the residuals χ^2 was minimized:

$$\chi^2 = \sum_{r=1}^n \left[\sum_q (S_r^{\text{meas.}} - S_r)^2 \right],$$

where $S_j^{\text{meas.}}$ represents actual data points and n is either two or four. The best fit constants, along with their 95% confidence intervals, are listed in Table III. The confidence intervals were obtained using the bootstrap method.⁸² This method requires minimal knowledge of the errors associated with each data point, because it uses the distribution of the data points themselves to estimate error (see BB for more details on our implementation of the bootstrap method). Since the fitting algorithm is based on nonlinear least squares, the best fit value does not necessarily lie in the center of the interval.

TABLE III. The material parameters for our coarse-grained implicit solvent model (CG) and the MARTINI force field simulation (DPPC). The values of $\{k_\lambda, k_c, k_A/b_0^2, \Omega/b_0, \kappa_\theta, \kappa_{tw}\}$ are the best fit values to the thermal fluctuation spectra. The 95% confidence intervals are written in parenthesis. The monolayer thickness b_0 for CG and DPPC is 2.4 nm and 1.8 nm, respectively. A value of k_A was also extracted by measuring the variance in the simulation box size, Eq. (46). All constants are defined with respect to the monolayer and c_0 is defined as the monolayer *total* spontaneous curvature. Care must be taken when comparing these quantities to earlier studies where conventions sometimes differ (see Table II for a discussion of the conventions used in BB). c_0 was calculated by using the best fit value for k_c combined with the first moment of the stress profile, Eq. (47).

System	Method	k_λ ($\frac{10^{-20}\text{J}}{\text{nm}^4}$)	k_c (10^{-20}J)	k_A ($\frac{10^{-20}\text{J}}{\text{nm}^2}$)	Ω ($\frac{10^{-20}\text{J}}{\text{nm}}$)	κ_θ ($\frac{10^{-20}\text{J}}{\text{nm}^2}$)	κ_{tw} (10^{-20}J)	c_0 (nm^{-1})
CG	Spectra	20(19–23)	16(15–21)	19(14–22)	16(13–22)	2.6(2.5–2.6)	1.1(1.0–1.1)	0.10
	Area Fluctuations			8.7				
DPPC	Spectra	43(40–44)	6.7 (6.6–11)	26 (20–27)	9.9(0–11)	5.4(5.3–5.4)	0.77(0.72–0.80)	–0.02
	Area Fluctuations			21				

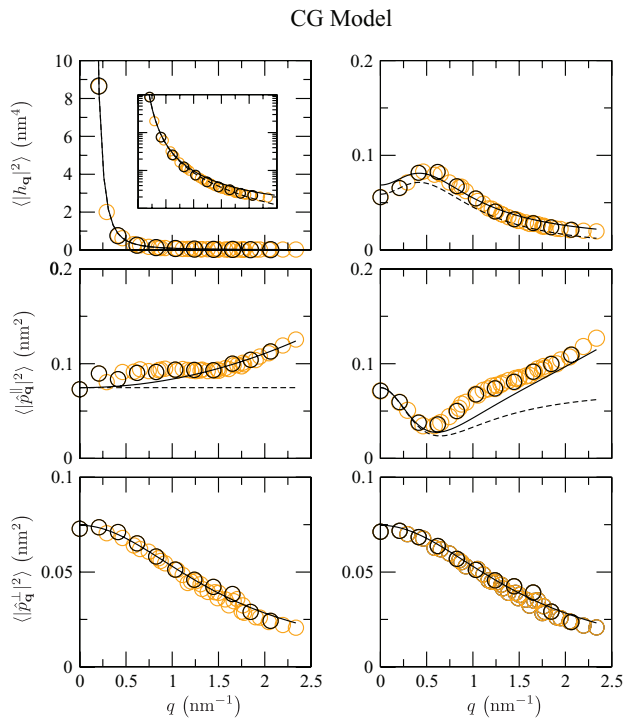


FIG. 9. Height $\langle |h_q|^2 \rangle$, thickness $\langle |t_q|^2 \rangle$, and tilt $\langle |\hat{p}_q^\perp|^2 \rangle$, $\langle |\bar{p}_q^\parallel|^2 \rangle$, $\langle |\hat{p}_q^\perp|^2 \rangle$ fluctuations for the CG model. Simulation data are displayed as circles. The data points used for the fits (black) are evenly spaced along the q_x and q_y axes. Data points which do not lie on the axes are shown in orange. The solid curves represent best fits of the data to Eqs. (39)–(43) with $\gamma_\lambda = 0$. Fit parameters are listed in Table III. $\langle |h_q|^2 \rangle$ is also plotted on a semi-log scale in the inset. Dashed curves correspond to the protrusion-free limit by using Eqs. (39)–(42) and the same values in Table III but with $k_\lambda \rightarrow \infty$. While only a small contribution to the height and thickness modes, protrusions are essential for explaining the qualitative behavior of $\langle |\bar{p}_q^\parallel|^2 \rangle$ and $\langle |\hat{p}_q^\perp|^2 \rangle$.

The low- q data for $\langle |h_q|^2 \rangle$ thus highly weights some of the fit parameters toward one side.

The average monolayer thickness b_0 was measured by calculating the mean bilayer thickness at each time step, averaging over all frames, and dividing by two. The values for CG and DPPC are 2.4 nm and 1.8 nm, respectively.

The thermal fluctuation spectra for both simulations are shown in Figs. 9–11. The data from CG and DPPC are in qualitative agreement with each other and both models are in excellent quantitative agreement with our analytic model. We also examined the behavior of the cross terms $\langle h_q \hat{p}_{-q}^\parallel \rangle$ and $\langle t_q \hat{p}_{-q}^\parallel \rangle$ in Fig. 11. Both the theory and simulation data show that these spectra are purely imaginary. Despite the fact that these data sets were not part of the fitting procedure, the curves match the data quite well.

In MNK, the tilt fluctuations within a single monolayer were measured but could not be quantitatively explained. Within our model, the monolayer tilt spectra averaged over all directions (as measured in MNK) $\langle |\tilde{m}_q^{(\alpha)}|^2 \rangle$ are naturally expressed by adding up the separate contributions of the measured peristaltic, undulation, longitudinal, and transverse modes:

$$\langle |\tilde{m}_q^{(\alpha)}|^2 \rangle = \frac{1}{2} (\langle |\hat{p}_q^\perp|^2 \rangle + \langle |\bar{p}_q^\parallel|^2 \rangle + \langle |\hat{p}_q^\parallel|^2 \rangle + \langle |\bar{p}_q^\perp|^2 \rangle).$$

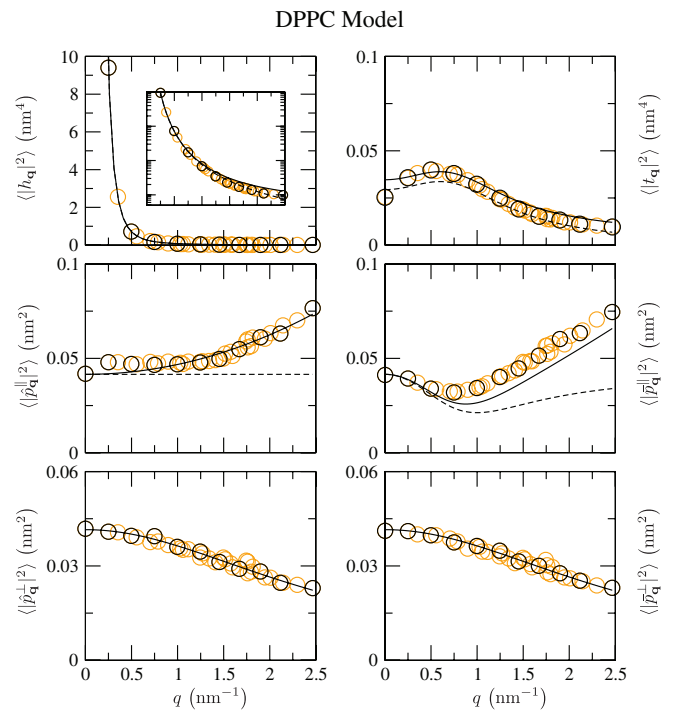


FIG. 10. Fluctuations and fits to the DPPC model. See Fig. 9 for details.

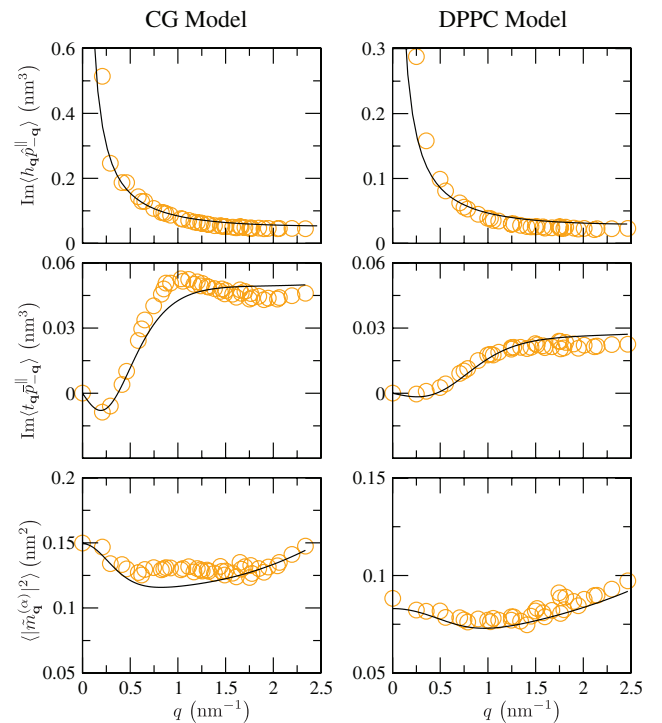


FIG. 11. Though not used in the fitting procedure, the data for $\langle h_q \hat{p}_{-q}^\parallel \rangle$, $\langle t_q \hat{p}_{-q}^\parallel \rangle$ and $\langle |\tilde{m}_q^{(\alpha)}|^2 \rangle$ agree with the theoretical predictions very closely. Both the theory and data show that the fluctuations in the cross-terms are purely imaginary. This may be understood mathematically since $\hat{p}_q^* = -\hat{p}_{-q}^\parallel$ and $h_q^* = h_{-q}$ and similarly for the peristaltic term (see Sec. III). The monolayer tilt averaged over all directions $\langle |\tilde{m}_q^{(\alpha)}|^2 \rangle$ is also plotted in MNK.

In Fig. 11, we plot the measured values of $\langle |\tilde{m}_{\mathbf{q}}^{(\alpha)}|^2 \rangle$ along with the theoretical prediction. Again the agreement is very good.

The values of k_A and k_c obtained from the fits may be compared with previous measurements. In BB, fitting the height and thickness spectra gave $k_A = 35 \times 10^{-20}$ J/nm². However, we believe our current value of k_A as obtained by fitting the spectra to be more precise since the theory and simulation values closely match at $q = 0$.

The area compressibility modulus may be extracted by measuring fluctuations in the box size⁸³

$$\frac{k_B T}{2k_A} = \left\langle \frac{(L - L_0)^4}{L^2} \right\rangle. \quad (46)$$

The corresponding values are listed in Table III. Within error bars, the value for DPPC agrees with the value obtained by fitting the spectra. Using the same MARTINI force field, a value of $k_A = 37 \times 10^{-20}$ J/nm² was found by measuring the slope of a stress-strain curve.⁸⁴ For CG, there is a larger disparity between the values of k_A as measured through Eq. (46) versus spectra fitting.

For both systems, the difference between the two measurements may stem from two issues. The value of k_A as determined by box size fluctuations depends on the size of the system.^{49,85} The discrepancies may also be rooted in our assumptions about volume conservation (BB). Real lipid systems are not strictly incompressible, so that Eq. (A5) is only an approximation. Though the portion of the theory involving thickness fluctuations is still correct, the k_A prefactor of the $(z^-)^2$ term in the Hamiltonian should not be called the area compressibility modulus, but really the thickness modulus.

The most commonly measured parameter is the bending rigidity k_c . Though our CG simulation is nearly the same as in BB, the value we find for k_c is larger than previously inferred ($k_{c, \text{monolayer}}^{\text{BB}} = 7 \times 10^{-20}$ J) by a factor of two. The discrepancy is not due to differences in the simulations; the data from the present simulations is very nearly identical to that obtained in BB (for those quantities measured in BB) and it was verified that fitting the new data as prescribed in BB reproduced the previous results. The discrepancy is due to the fact that our simulated membranes are too small for $\langle |h_{\mathbf{q}}|^2 \rangle_{\text{meas}}$ to reach the asymptotic $\propto q^{-4}$ regime over a large range of wavevectors. Discrepancies in the functional forms used to fit the data (compare BB to the present theory) yield significantly different “best fits” for k_c when the available data is limited to short and intermediate length scales. This effect was also noted in MNK. A similar outcome is present, though less severe, for DPPC. The monolayer bending modulus has been measured as 4×10^{-20} J by fitting the height fluctuations to Eq. (37).⁸⁴ For the same system, $k_c = 6 \times 10^{-20}$ J was also calculated by measuring the system size-dependent value of the area compressibility modulus.⁸⁴

Knowing the bending modulus, we can calculate the value of the monolayer spontaneous total curvature c_0 as an integral over the bilayer stress profile:⁶⁵

$$k_c c_0 = -\frac{1}{2} \int s(z) |z| dz, \quad (47)$$

where the integration is over the entire bilayer, centered at $z = 0$. It should be noted that the profile obtained in this work (Fig. 6) is qualitatively different than that reported in the original study of the CG model⁴⁵ due to our adoption in this work of a commonly employed definition for the pressure tensor. The original definition was not standard and was chosen for convenience in dealing with the rigid constraints employed in the original version of the CG model. Though the microscopic definition of the pressure is not unique⁸⁶ and depends on the choice of the integration contour, Sonne *et al.*⁸¹ have shown that the two conventions used in this paper yield consistent results for planar bilayers (see Sec. IV B). The values of c_0 are given in Table III. The value of c_0 for CG is smaller than the previous value⁸⁷ by a factor of two since our new measurement of k_c is twice as big. The differences in shape of the stress profile between CG and BB, as mentioned above, do not contribute significantly to the disparity in c_0 between the two studies.

Experimentally, the spontaneous curvature of DPPC is very small and difficult to measure. Our measurement of c_0 falls within the range reported in the original MARTINI study of DPPC.⁵⁵

For each system, the distance d from $z^{(m)}$ to the neutral surface of each monolayer may be determined from Eq. (23). Using the values from Table III, we find $d/b_0 = 0.68$ and $d/b_0 = 0.60$ for CG and DPPC, respectively. These numbers lie within the range of values required to explain the membrane dynamics observed with neutron spin echo spectroscopy.⁸⁸

In terms of protrusions, the $\gamma_\lambda = 0$ approximation fits the data quite well. When fitting the CG data to Eqs. (39)–(42) while allowing γ_λ to vary, its optimal value was nearly zero already. This result was not necessarily implied by the fact that our CG model does not contain explicit solvent. As described by Brannigan, Philips, and Brown,⁴⁵ solvent effects are captured by incorporating a strong attraction between interface beads, which serves to mimic the hydrophobic effect (see Fig. 6). Fitting the DPPC data resulted in values of $\gamma_\lambda = 2.3 \times 10^{-20}$ J/nm² and $k_\lambda = 26 \times 10^{-20}$ J/nm⁴ along with the other constants being same as those in Table III. The resulting curves were nearly identical to those shown in Figs. 10 and 11. Fixing $\gamma_\lambda = 0$ required that $k_\lambda = 43 \times 10^{-20}$ J/nm⁴ in order to maintain the best fits to the tilt fluctuations parallel to \mathbf{q} .

The individual spectra for $\hat{\mathbf{p}}$ and $\bar{\mathbf{p}}$ have not been previously measured. Though obtaining the normals to each surface required manipulations in discrete Fourier space, we found the tilt spectra to be only weakly dependent on the grid size. As expected, the behavior of $\langle |\hat{p}_{\mathbf{q}}^\perp|^2 \rangle$ and $\langle |\bar{p}_{\mathbf{q}}^\perp|^2 \rangle$ remains the same on length scales below the bilayer thickness. As shown in Figs. 9 and 10, a finite value of k_λ is needed to explain the rise in $\langle |\hat{p}_{\mathbf{q}}^\parallel|^2 \rangle$ and $\langle |\bar{p}_{\mathbf{q}}^\parallel|^2 \rangle$ as q increases.

As mentioned earlier, the tilt modulus of a lipid membrane has only been indirectly determined experimentally. From the DPPC data we find $\kappa_\theta = 5.4 \times 10^{-20}$ J/nm², in good agreement with the value obtained by MNK ($\kappa_\theta \approx 5 \times 10^{-20}$ J/nm²) (though the same MARTINI force fields were used, the small difference may be due to a number of details related to the simulation setup and curve fitting method). The

value 5×10^{-20} J/nm² is roughly equal to the surface tension between hydrocarbons and water.

Intermonolayer coupling may be investigated by comparing the values of the undulation and peristaltic tilt modes at $q = 0$. If coupling were present, fluctuations in the tilt undulations $\langle |\hat{p}_{\mathbf{q}}^{\parallel}|^2 \rangle$, $\langle |\hat{p}_{\mathbf{q}}^{\perp}|^2 \rangle$ would be different from those of peristaltic tilt $\langle |\bar{p}_{\mathbf{q}}^{\parallel}|^2 \rangle$, $\langle |\bar{p}_{\mathbf{q}}^{\perp}|^2 \rangle$. Since they are virtually the same at $q = 0$, the effect of intermonolayer coupling is negligible.

To our knowledge, this is the first time the twist modulus of a membrane has been measured in terms of simulations or experiment. For both CG and DPPC, its value is small compared to k_c , which is consistent with qualitative predictions.¹⁷

VI. CONCLUSION

Starting from a physically motivated model for the membrane deformation energy, we derived expressions for the thermal fluctuations of several quantities involving height, thickness, and lipid orientation. These expressions were found to be in excellent agreement with molecular simulations over both the macroscopic and protrusion regimes.

Analyzing the thermal fluctuations in terms of longitudinal and transverse modes allowed us to individually probe the nature of two new effects. First, we showed that twist deformations are indeed present, whose energetic cost is on the order of a few $k_B T$. Second, the analysis demonstrated that the measured tilt vectors are affected by gradients in the protrusion field.

We have found that modeling protrusions as harmonically constrained fluctuations at the lipid/water interface quantitatively describes the simulation data. For the systems we studied, it was found that the protrusion-related surface tension γ_λ could be approximated as vanishing, meaning that protrusions could be modeled with just one parameter: k_λ . Within the $\gamma_\lambda = 0$ approximation, our predicted fluctuation spectrum resembles expressions from previous models^{11,44} in which $\gamma_\lambda \neq 0$ but no tilt is present. This may be understood by examining the height spectra. In BB, the expression for $\langle |h_{\mathbf{q}}|^2 \rangle$ in the decoupled protrusion/bending regime is given by

$$\langle |h_{\mathbf{q}}|^2 \rangle = \frac{k_B T}{2} \left(\frac{1}{k_c q^4} + \frac{1}{(k_\lambda + \gamma_\lambda q^2)} \right),$$

which accurately accounts for the non- q^{-4} behavior. With $\gamma_\lambda = 0$, our model predicts

$$\langle |h_{\mathbf{q}}|^2 \rangle = \frac{k_B T}{2} \left(\frac{1}{k_c q^4} + \frac{1}{\kappa_\theta q^2} + \frac{1}{k_\lambda} \right).$$

Here, it is the coupling between height and tilt fluctuations which gives rise to the non- q^{-4} behavior. For the systems we have studied, both expressions fit the data very well down to length scales of a few nanometers; it does not seem possible to validate one model over the other solely on the basis of the simulated height fluctuation data available to us. Nevertheless, we believe that Eq. (39) is preferable to the expression

in BB, due to the underlying physical motivation based on molecular tilt and the fact that the tilt modulus κ_θ appearing in Eq. (39) is consistent with the value extracted from the tilt fluctuations for both systems we studied.

We briefly mention that an interesting recent paper by Brandt and co-workers⁸⁹ suggests an alternative method to analyzing bilayer simulation data, quite different from that employed by us and detailed in Appendix C. The method proposed by these workers is based upon a “direct” analysis of the simulation data in Fourier space, without interpolating the lipid positions to a real-space grid. Although both methodologies produce similar results in the small q limit, at intermediate q values the method from Brandt *et al.* yields spectra without any signature of $1/q^2$ contributions to the height spectrum $\langle |h_{\mathbf{q}}|^2 \rangle$ (both for the systems studied in that work and we have verified similar behavior using their methods in the analysis of our simulations). We have no explanation for these results at present. The real-space analysis employed here (and by other workers previously) appears consistent with the theoretical predictions. The direct Fourier method of Brandt *et al.*⁸⁹ does not appear to be consistent with our theoretical results.

Though our model takes the overall orientation of the lipids into account, it does not contain information about the relative positions of the two hydrocarbon tails. For example, each DPPC molecule may be also characterized by a vector pointing from one tail to the other, so that viewed from above, the membrane consists of a collection of ellipses rather than circles. Though this level of detail was not required to explain any of the observables for DPPC examined here, the tail-tail orientation may be important for building a more comprehensive model for membrane structure in the future.

By incorporating the effects of molecular orientation, this model is considerably more general than our previous one (BB). However, the number of additional material constants is minimal. In the earlier theory, five moduli appeared in the Hamiltonian: $\{k_c, k_A, \zeta, k_\lambda, \gamma_\lambda\}$. Our current model includes the added orientational parameters κ_θ and κ_{tw} . For the two lipid systems we analyzed, it was found that neglecting surface tension contributions to the protrusion energy ($\gamma_\lambda = 0$) resulted in excellent agreement with the data, reducing the size of our parameter set to six. Excluding the completely new effect of twist, whose modes are decoupled from the rest of the free energy, our model for CG and DPPC contains exactly the same number of parameters as before: $\{k_c, k_A, \Omega, k_\lambda, \kappa_\theta\}$, yet provides predictions for a completely new class of observables related to molecular orientation.

ACKNOWLEDGMENTS

E.P. would like to acknowledge communication with G. Brannigan and discussions with G. Bellesia. This material is based upon work supported by the National Science Foundation (NSF) under Grant Nos. DMR 0520415 and CHE 0848809. TeraGrid resources were provided by the TACC under Grant No. TG-MCB080142N. Financial support provided by the Los Alamos National Laboratory Institute for Multiscale Materials Studies, operated under the auspices of the National Nuclear Security Administration of the U. S.

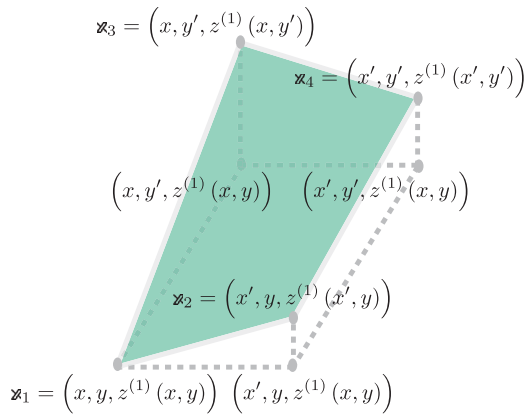


FIG. 12. The upper bounding surface of $dV^{(1)}$ is $z^{(1)}$ (green), which contains \mathbb{x}_1 , \mathbb{x}_2 , \mathbb{x}_3 , and \mathbb{x}_4 .

Department of Energy (DOE) under contract No. DE-AC52-06NA25396. F.L.H.B. is a Camille Dreyfus Teacher-Scholar.

APPENDIX A: VOLUME AND AREA ELEMENTS

Here we derive general expressions for the effective thickness $g_V^{(\alpha)}$, interfacial area per molecule $\Sigma^{(\alpha)}$, and head group area per molecule $\Sigma_h^{(\alpha)}$ up to quadratic order.

The effective thickness $g_V^{(\alpha)}$ is needed in Eq. (14) in order to convert an integral over lipids into an integral over area. $g_V^{(\alpha)}$ is also used for deriving general expressions for $\Sigma^{(\alpha)}$ and $\Sigma_h^{(\alpha)}$. For the top layer, $v dn^{(1)} = dV^{(1)} = g_V^{(1)} d\mathbf{r}$, where v is the volume per molecule and $dn^{(1)}$ is the number of lipids whose projected polar-nonpolar interfaces are located within (x, y) , $(x + dx, y)$, $(x, y + dy)$, and $(x + dx, y + dy)$ (Fig. 12). For quantities $g(x, y)$ evaluated at $(x + dx, y)$, we take $g(x + dx, y) \approx g(x, y) + \partial g/\partial x|_y dx$ and similarly for $(x, y + dy)$ and $(x + dx, y + dy)$. We discard all terms containing $(dx)^2$ or $(dy)^2$.

The region $dV^{(1)}$ may be decomposed into five tetrahedrons. A tetrahedron has four vertices, four faces, and several standard volume formulas. We describe each tetrahedron by its vertices: $(\mathbb{x}_5, \mathbb{x}_1, \mathbb{x}_7, \mathbb{x}_6)$, $(\mathbb{x}_8, \mathbb{x}_4, \mathbb{x}_6, \mathbb{x}_7)$, $(\mathbb{x}_2, \mathbb{x}_6, \mathbb{x}_4, \mathbb{x}_1)$,

$(\mathbb{x}_3, \mathbb{x}_7, \mathbb{x}_1, \mathbb{x}_4)$, and $(\mathbb{x}_1, \mathbb{x}_4, \mathbb{x}_7, \mathbb{x}_6)$. The volume of a tetrahedron with vertices located at $(\mathbb{x}_A, \mathbb{x}_B, \mathbb{x}_C, \mathbb{x}_D)$ is given by

$$V = \frac{1}{6} (\mathbb{x}_C - \mathbb{x}_A) \cdot [(\mathbb{x}_B - \mathbb{x}_A) \times (\mathbb{x}_D - \mathbb{x}_C)].$$

The expression is positive as long as \mathbb{x}_B , \mathbb{x}_C , and \mathbb{x}_D are oriented counterclockwise as viewed from \mathbb{x}_A . This method is accurate up to quadratic order:

$$\frac{g_V^{(\alpha)}}{b_0} = 1 + \frac{b^{(\alpha)} - b_0}{b_0} + \frac{b_0}{2} \nabla \cdot \mathbf{n}^{(\alpha)} + (b^{(\alpha)} - b_0) \nabla \cdot \mathbf{n}^{(\alpha)} - \frac{1}{2} |\mathbf{n}^{(\alpha)}|^2 + \frac{b_0^2}{3} \det \left(\frac{\partial n_j^{(\alpha)}}{\partial r_k} \right) + \mathbf{n}^{(\alpha)} \cdot \nabla z^{(\alpha)}. \quad (\text{A1})$$

This result is an extension of the expression for $g_V^{(\alpha)}$ given by May and Ben-Shaul.²¹ The final term takes the gradient of the “anchoring” surface into account, which was originally assumed to be flat.²¹ When $\nabla z^{(\alpha)} = 0$, Eq. (A1) reduces back to their result with the exception of the prefactor of the saddle-splay term. The previous study contained a factor of 1/2 instead of 1/3. This discrepancy appears to be the result of a small error in the expression for “ dV_C ” within the appendix.²¹

The quantities $g_V^{(\alpha)}$ can be used to calculate the area per molecule at any surface. Up to second order, the infinitesimal area of the top surface shown in Fig. 12 is

$$dA^{(\alpha)} = \left\{ 1 + \frac{1}{2} (\nabla z^{(\alpha)})^2 \right\} d\mathbf{r} \equiv g_A^{(\alpha)} d\mathbf{r}. \quad (\text{A2})$$

In order to express Eqs. (A1) and (A2) in terms of $\mathbf{m}^{(\alpha)}$, we demand that the vectors $b^{(\alpha)} \mathbf{m}^{(\alpha)}$ extend from $z^{(\alpha)}$ to $z^{(m)}$. For the top monolayer, this implies

$$z^{(1)} - z^{(m)} = b^{(1)} \mathbf{m}^{(1)} \cdot (\nabla z^{(m)}, -1). \quad (\text{A3})$$

Expanding Eq. (A3) up to second order gives the useful relation

$$|\mathbf{m}^{(1)}|^2 = \mathbf{n}^{(1)} \cdot (\mathbf{n}^{(1)} - 2\nabla z^{(m)} - 2\nabla b^{(1)}) + (\nabla z^{(1)})^2. \quad (\text{A4})$$

Using the second-order expressions for $g_V^{(\alpha)}$ and $g_A^{(\alpha)}$, the area per molecule $dA^{(\alpha)}/dn^{(\alpha)}$ reads as

$$\frac{\Sigma^{(\alpha)} - \Sigma_0}{\Sigma_0} = -\frac{b^{(\alpha)} - b_0}{b_0} + \left(\frac{b^{(\alpha)} - b_0}{b_0} \right)^2 - \frac{b_0}{2} \nabla \cdot \mathbf{n}^{(\alpha)} + \frac{b_0^2}{4} (\nabla \cdot \mathbf{n}^{(\alpha)})^2 + \frac{1}{2} |\mathbf{m}^{(\alpha)}|^2 - \frac{b_0^2}{3} \det \left(\frac{\partial n_j^{(\alpha)}}{\partial r_k} \right). \quad (\text{A5})$$

This is the equation of state of a single molecule, which gives the relationship between the variables $\{\Sigma^{(\alpha)}, b^{(\alpha)}, \mathbf{m}^{(\alpha)}, \mathbf{n}^{(\alpha)}\}$ under the assumption of constant lipid chain volume. It generalizes Eq. (6.19) from Safran,⁶⁵ which relates the chain length to the mean curvature H and Gaussian curvature K assuming $\Sigma^{(\alpha)} = \Sigma_0$ and $\mathbf{m}^{(\alpha)} = 0$. Under these conditions, Eq. (A5) reduces back to Safran’s result using the second-order approximations $2H = \nabla \cdot \mathbf{N}$ and $K = \det(\partial N_j/\partial r_k)$.

The area per molecule within the head group region $\Sigma_h^{(\alpha)}$ is calculated as follows. Here we again refer to the upper

monolayer. The distance ℓ_h from the polar-nonpolar interface to the head group is assumed to be constant. Just as the vectors $b^{(1)} \mathbf{m}^{(1)}$ extend from $z^{(1)}$ to $z^{(m)}$ (Fig. 13), the vectors $-\ell_h \mathbf{m}^{(1)}$ extend from $z^{(1)}$ to the head group surface (Fig. 14). In the infinitesimal limit, the points $(\mathbb{x}_9, \mathbb{x}_{10}, \mathbb{x}_{11}, \mathbb{x}_{12})$ are coplanar. The area of the corresponding quadrilateral is given by

$$A = \frac{1}{2} |(\mathbb{x}_9 - \mathbb{x}_{11}) \times (\mathbb{x}_{10} - \mathbb{x}_{12})|.$$

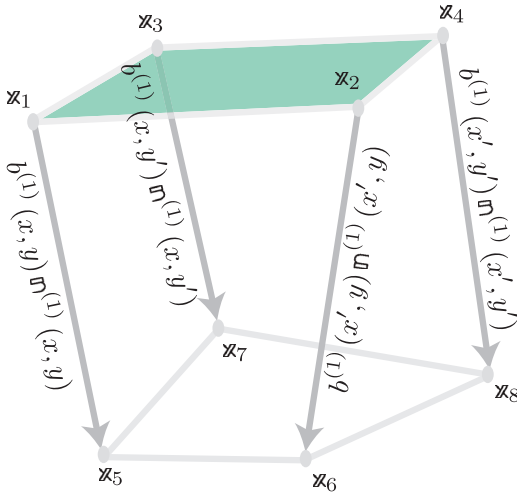


FIG. 13. The infinitesimal volume element $dV^{(1)}$. The bottom vertices ($\mathbb{X}_5, \mathbb{X}_6, \mathbb{X}_7, \mathbb{X}_8$) are located at the end of the lipid tails whose polar-nonpolar interfaces lie at ($\mathbb{X}_1, \mathbb{X}_2, \mathbb{X}_3, \mathbb{X}_4$), respectively. For graphical clarity we write $x' \equiv x + dx$ and $y' \equiv y + dy$. $z^{(1)}$ is shown in green.

Up to quadratic order in $\nabla \mathbf{n}^{(\alpha)}$ and $\nabla z^{(\alpha)}$, the infinitesimal area element is

$$dA_h^{(\alpha)} = g_{A_h}^{(\alpha)} d\mathbf{r} = \left[1 - \ell_h \nabla \cdot \mathbf{n}^{(\alpha)} + \ell_h^2 \det \left(\frac{\partial n_j^{(\alpha)}}{\partial r_k} \right) + \frac{1}{2} (\nabla z^{(\alpha)})^2 \right] d\mathbf{r}. \quad (\text{A6})$$

This expression generalizes the second-order result for parallel surfaces,⁶⁵ in which $\mathfrak{m}^{(\alpha)} = \mathbb{N}^{(\alpha)}$. Using Eqs. (A1) and (A6), the head group area is given by

$$\begin{aligned} \frac{\Sigma_0}{\Sigma_h^{(\alpha)}} &= 1 + \frac{b^{(\alpha)} - b_0}{b_0} + \left(\frac{b_0}{2} + \ell_h \right) \nabla \cdot \mathbf{n}^{(\alpha)} \\ &+ (b_0 + \ell_h) \left(\frac{b^{(\alpha)} - b_0}{b_0} \right) \nabla \cdot \mathbf{n}^{(\alpha)} + \ell_h^2 (\nabla \cdot \mathbf{n}^{(\alpha)})^2 \\ &- \frac{1}{2} |\mathfrak{m}^{(\alpha)}|^2 + \left(\frac{b_0^2}{3} - \ell_h^2 \right) \det \left(\frac{\partial n_j^{(\alpha)}}{\partial r_k} \right). \end{aligned} \quad (\text{A7})$$

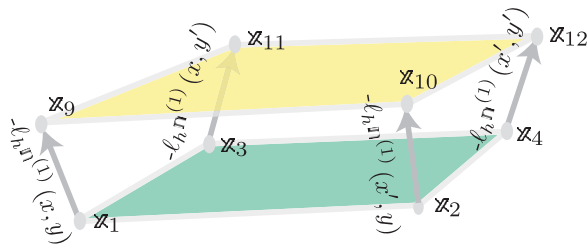


FIG. 14. $-\ell_h \mathfrak{m}^{(1)}$ extends from $z^{(1)}$ (green) to the head group surface (yellow). The coloring corresponds to Fig. 3.

To derive Eq. (12), Eqs. (A5) and (A7) are substituted into Eq. (11), followed by using the first order version of Eq. (A5),

$$\frac{b^{(\alpha)} - b_0}{b_0} = -\frac{\Sigma^{(\alpha)} - \Sigma_0}{\Sigma_0} - \frac{b_0}{2} \nabla \cdot \mathbf{n}^{(\alpha)},$$

to express the quadratic contributions containing $(b^{(\alpha)} - b_0)$ in terms of $(\Sigma^{(\alpha)} - \Sigma_0)$ and $\nabla \cdot \mathbf{n}^{(\alpha)}$. The elastic constants in Eq. (12) are related to the microscopic parameters in Eq. (11) through

$$\begin{aligned} k_A &= 2 \left(\gamma_s + \frac{\tau b_0^2}{\Sigma_0} \right), \\ \kappa_\theta &= \gamma_s - \frac{B}{\Sigma_0^2}, \\ k_c^\Sigma &= \frac{B}{\Sigma_0^2} (2\ell_h^2 - \ell_h b_0 - b_0^2) + b_0^2 \gamma_s \left(1 + \frac{\tau b_0^2}{2\gamma_s \Sigma_0} \right), \\ k_c^\Sigma c_0 &= \frac{B \ell_h}{\Sigma_0^2} - \frac{b_0^3 \tau}{\Sigma_0} + \frac{b_0^2 \ell_c \tau}{\Sigma_0}, \\ \mu &= -\frac{B}{\Sigma_0} (b_0 + \ell_h) + b_0 \gamma_s + \frac{\tau b_0^3}{\Sigma_0}, \\ k_G &= \frac{B}{\Sigma_0^2} \left(\frac{b_0^2}{3} - \ell_h^2 \right) - \frac{b_0^2 \gamma_s}{3}. \end{aligned} \quad (\text{A8})$$

The first two expressions are identical to those given by May.²² Due to different conventions, the expressions for all elastic constants involving curvature are not the same. For $k_c^\Sigma, k_c^\Sigma c_0$, and μ , these differences originate from two sources. First, we expressed the free energy per molecule in terms of $\Sigma^{(\alpha)}$ rather than $b^{(\alpha)}$. This leads to a renormalization of the prefactors involving $\nabla \cdot \mathbf{n}^{(\alpha)}$. Second, the geometries are defined in terms of different surfaces. Our director field points from $z^{(\alpha)}$ toward the membrane interior, as opposed to pointing outward from the midplane. Within each convention, $\Sigma_h^{(\alpha)}$ and $\Sigma_i^{(\alpha)}$ depend on the effective curvature of each corresponding director field a different way. Despite the issues connecting our parameters to a specific microscopic model, the functional forms of Eqs. (A5) and (A7) are identical to those in May.²²

Within our formalism, the director field may also be defined with respect to the midplane. Expressing the free energy per molecule in terms of $b^{(\alpha)}$, the expressions for the elastic constants may be shown to exactly match May's.²² For the upper monolayer, this may be accomplished by effectively flipping Figs. 12 and 13 upside-down, so that ($\mathbb{X}_1, \mathbb{X}_2, \mathbb{X}_3, \mathbb{X}_4$) are located within the midplane, while ($\mathbb{X}_5, \mathbb{X}_6, \mathbb{X}_7, \mathbb{X}_8$) belong to the polar-nonpolar interface. We may define $\nu d\check{r}^{(1)} = d\check{V}^{(1)} = \check{g}_V^{(1)} d\mathbf{r}$, where $d\check{r}^{(1)}$ is the number of lipids whose chain ends are located within the area element $d\mathbf{r}$. The expression for $\check{g}_V^{(1)}$ is identical to Eq. (A1) but with $\mathbf{n}^{(1)}$ replaced by $\check{\mathbf{n}}^{(1)}$, the director field extending from the midplane. The factor $\check{g}_A^{(1)}$ may be found by calculating the area of the quadrilateral formed by ($\mathbb{X}_9, \mathbb{X}_{10}, \mathbb{X}_{11}, \mathbb{X}_{12}$):

$$\check{g}_{A_h}^{(1)} = 1 + \frac{1}{2}(\nabla z^{(1)})^2 + (b_0 + \ell_h) \nabla \cdot \check{\mathbf{n}}^{(1)} + \nabla \cdot [\check{\mathbf{n}}^{(1)}(b^{(1)} - b_0)] + (b_0 + \ell_h)^2 \det \left(\frac{\partial \check{n}_j^{(1)}}{\partial \check{r}_k} \right). \quad (\text{A9})$$

This expression is a further generalization of Eq. (A6) since the distance between the midplane and the surface formed by the heads is allowed to vary. We may easily obtain $\check{g}_{A_i}^{(1)}$ from Eq. (A9) by setting $\ell_h = 0$. Calculating $\Sigma_h^{(1)}$ and $\Sigma_i^{(1)}$ in terms of $\check{g}_V^{(1)}$, $\check{g}_{A_h}^{(1)}$, and $\check{g}_{A_i}^{(1)}$ and plugging them into Eq. (11) yields the same expressions for the elastic constants as those in Ref. 22 (noting the prefactor issue mentioned after Eq. (A1)).

APPENDIX B: COMMENTS ON THE TILT FREE ENERGY

In terms of the microscopic parameters given in Eq. (11), the tilt modulus may be written as (see Eq. (A8))

$$\kappa_\theta = \gamma_s - \frac{B}{\Sigma_0^2} = \frac{2b_0\tau}{\Sigma_0} (b_0 - \ell_c), \quad (\text{B1})$$

where the second equality follows from the equilibrium condition mentioned under Eq. (12). From Eq. (B1), we see that if $b_0 = \ell_c$ or $\tau = 0$, it follows that $\kappa_\theta = 0$, meaning that the energetic cost of tilt deformations originates from the chain-stretching term in Eq. (11). Though not present in the original opposing forces model,¹² May and Ben-Shaul included the third term in Eq. (11) in order to account for the energetic cost of tilt.²¹

From Eqs. (A8) and (B1), it can be shown that the material constants are expected to obey certain inequalities. For monolayers in which $\mathbf{m}^{(\alpha)} = 0$ is the preferred orientation, it is required that $b_0 > \ell_c$ in order for $\kappa_\theta > 0$. Otherwise, the lipids would find tilting away from the surface normal to be energetically preferable to alignment with the surface normal. Also, $k_A > 2\kappa_\theta$ and $\kappa_\theta < \gamma_s$ from Eq. (A8).

Compared to curvature, the tilt term in our macroscopic Hamiltonian is less cumbersome when switching between different sets of variables. Though the free energy in Eq. (13) was written in terms of $\{\Sigma^{(\alpha)}, \nabla \cdot \mathbf{n}^{(\alpha)}, \mathbf{m}^{(\alpha)}\}$, it may be expressed in terms of $\{b^{(\alpha)}, \nabla \cdot \mathbf{n}^{(\alpha)}, \mathbf{m}^{(\alpha)}\}$ using Eq. (A5),

$$\begin{aligned} \frac{\check{f}^{(\alpha)}}{\Sigma_0} &= \frac{k_A}{2} \left(\frac{b^{(\alpha)} - b_0}{b_0} \right)^2 + \left(\frac{k_c^\Sigma}{2} - \frac{b_0\mu}{2} + \frac{k_A b_0^2}{8} \right) (\nabla \cdot \mathbf{n}^{(\alpha)})^2 \\ &+ k_c^\Sigma c_0 \nabla \cdot \mathbf{n}^{(\alpha)} + \left(\frac{k_A b_0}{2} - \mu \right) \left(\frac{b^{(\alpha)} - b_0}{b_0} \right) \nabla \cdot \mathbf{n}^{(\alpha)} \\ &+ \frac{\kappa_\theta}{2} |\mathbf{m}^{(\alpha)}|^2 + \frac{\kappa_{tw}}{2} (\nabla \times \mathbf{m}^{(\alpha)})^2. \end{aligned} \quad (\text{B2})$$

While the coefficient of the $(\nabla \cdot \mathbf{n}^{(\alpha)})^2$ term has become renormalized, the coefficient of the tilt term is unchanged since $|\mathbf{m}^{(\alpha)}|$ only enters Eq. (A5) at second order. Hence our model contains only a single tilt modulus that appears in both representations, but two different curvature moduli, $\{k_c^b, k_c^\Sigma\}$ (see Sec. II B). Similarly, the model contains only a single twist modulus.

Though no direct experimental measurements of κ_θ are available so far, Hamm and Kozlov estimated a value of

$\kappa_\theta = 4 \times 10^{-20}$ J/nm² based on experimental data related to the temperature-induced transition of dioleoylphosphoethanolamine (DOPE) between the lamellar L_α and inverse-hexagonal phase H_{II} .³⁰

In addition to the ‘‘elastic’’ model of tilt presented here and in Refs. 14, 21, 22, and 30, purely entropic effects have also been discussed.⁹⁰ Including these contributions to the free energy results in a renormalization of the tilt modulus while leaving the rest of the Hamiltonian unaltered. Since the individual effects cannot be easily separated in terms of molecular simulation analysis, we consider the κ_θ appearing in our theory to reflect a combination of elastic and entropic effects.

APPENDIX C: NUMERICAL DISCRETIZATION PROCEDURE

All quantities are discretized onto a square $M \times M$ grid in the bilayer plane (x, y) where $M = 18$. Here, (x_ℓ, y_ℓ, z_ℓ) refers to the position of the interface point of the ℓ th lipid and $\hat{\mathbf{m}}_\ell$ is the unit vector pointing from (x_ℓ, y_ℓ, z_ℓ) to its corresponding tail point. The choice of how the interface points and tail points are defined for each lipid model is described in Sec. V.

The discretization procedure consists of the following steps:

(a) Determine the mean z -coordinate of all interface points: $\bar{z} = \frac{1}{N} \sum_{\ell=1}^N z_\ell$.

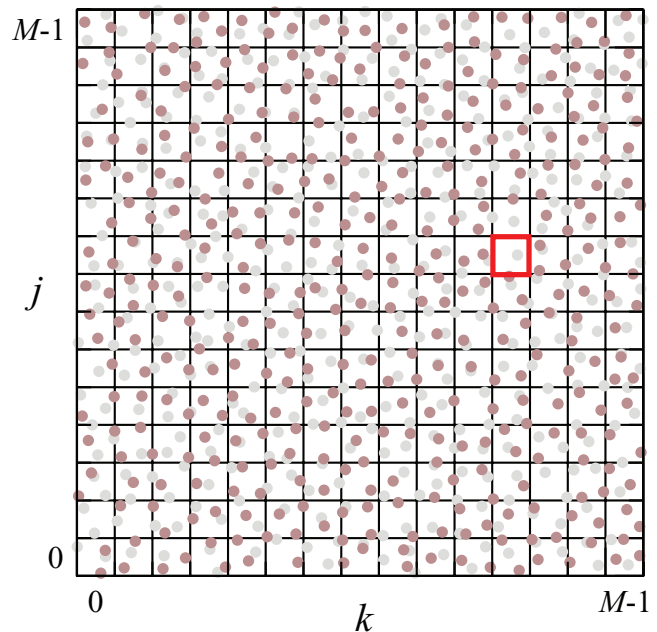


FIG. 15. Schematic of lipid assignment to a $M \times M$ grid. Filled circles represent lipid interface points (brighter: lipid in the lower monolayer; darker: lipid in upper monolayer). The highlighted square is an example of a patch that does not contain lipids in the upper monolayer ($n_{jk}^{(1)} = 0$).

(b) Divide lipids into upper and lower monolayers on the basis of \bar{z} :

upper monolayer : $z_\ell > \bar{z}$

lower monolayer : $z_\ell < \bar{z}$.

Once the lipids have been assigned to each monolayer, they are analyzed separately in the following steps.

(c) Assign lipids to a grid (Fig. 15). The ℓ th lipid is assigned to the patch with indices (j, k) , where $j, k = 0 \dots M - 1$ based on the xy -coordinates of its interface point according to the expression

$$(j, k)_\ell = (\lfloor x_\ell M/L \rfloor, \lfloor y_\ell M/L \rfloor), \quad (\text{C1})$$

where $\lfloor \dots \rfloor$ is the floor function. Assigning the average height of each patch to its lower left corner rather than its center amounts to an overall translation, which has no effect on the measured spectra in Fourier space (please note that the indices j and k in this appendix hold a different meaning than that introduced in Sec. II A).

(d) Calculate the average z -coordinate of each patch z_{jk} , relative to \bar{z} in terms of the number of lipids within that patch n_{jk} :

$$z_{jk} = \frac{1}{n_{jk}} \sum'_\ell z_\ell - \bar{z}, \quad (\text{C2})$$

where \sum' indicates summation only over the n_{jk} lipids in patch (j, k) .

(e) If a patch contains no lipids ($n_{jk} = 0$) as in Fig. 15, then a simple interpolation is performed. The z -coordinate is calculated as a weighted average from the nearest-neighbor grid points $\langle j, k \rangle = (j \pm 1, k \pm 1)$:

$$z_{jk} = \frac{\sum_{\langle j,k \rangle} n_{\langle j,k \rangle} z_{\langle j,k \rangle}}{\sum_{\langle j,k \rangle} n_{\langle j,k \rangle}}.$$

This method assumes that no two neighboring patches within the same monolayer are empty.

(f) Take the Fourier transform of z_{jk} using FFTW.⁹¹ Calculate $h_{\mathbf{q}}$ and $t_{\mathbf{q}}$ using Eq. (8).

(g) Calculate $(\nabla z)_{jk}$ to evaluate the surface normal

$$\tilde{\mathbf{N}}_{jk} \equiv \pm (\nabla z)_{jk} / \sqrt{(\nabla z)_{jk}^2 + 1}, \quad (\text{C3})$$

where (+) is used for the top monolayer and (−) is used for the bottom. The gradient is calculated in Fourier space as $(\nabla z)_{\mathbf{q}} = i\mathbf{q}z_{\mathbf{q}}$ and the inverse Fourier transform of $(\nabla z)_{\mathbf{q}}$ is used to obtain $(\nabla z)_{ij}$. Fourier components whose q_x or q_y values correspond to $n, m = -M/2$ (the Nyquist frequency) are disregarded.

(h) Compute the grid-averaged tilt vector $\tilde{\mathbf{m}}_{jk}$ given by

$$\tilde{\mathbf{m}}_{jk} = \frac{1}{n_{jk}} \sum'_\ell \tilde{\mathbf{n}}_\ell - \tilde{\mathbf{N}}_{jk},$$

where $\tilde{\mathbf{N}}_{jk}$ is given in Eq. (C3).

(i) Using the discrete Fourier transform, calculate $\{\hat{p}_{\mathbf{q}}^x, \hat{p}_{\mathbf{q}}^y, \bar{p}_{\mathbf{q}}^x, \bar{p}_{\mathbf{q}}^y\}$ defined in Eq. (10), where the superscripts denote the q_x and q_y components.

(j) Calculate $\{\hat{p}_{\mathbf{q}}^\perp, \bar{p}_{\mathbf{q}}^\perp\}$ using the transformation,

$$\begin{pmatrix} \hat{p}_{\mathbf{q}}^\parallel \\ \hat{p}_{\mathbf{q}}^\perp \end{pmatrix} = \frac{1}{q} \begin{pmatrix} q_x & q_y \\ -q_y & q_x \end{pmatrix} \begin{pmatrix} \hat{p}_{\mathbf{q}}^x \\ \hat{p}_{\mathbf{q}}^y \end{pmatrix},$$

and similarly for $\bar{p}_{\mathbf{q}}^\parallel$ and $\bar{p}_{\mathbf{q}}^\perp$.

(k) Average over all frames to acquire equilibrium averages $\langle \dots \rangle$.

(l) Obtain spectra which only depend on q by averaging data sets over \mathbf{q}' values for which $|\mathbf{q}'| = q$.

APPENDIX D: THERMAL AVERAGES FOR COUPLED BENDING/PROTRUSION MODES

Here, the expressions for the fluctuation spectra are given for the general case of coupled bending/protrusion modes (see Sec. III),

$$\langle |h_{\mathbf{q}}|^2 \rangle = \langle (z_{\mathbf{q}}^+ + \lambda_{\mathbf{q}}^+) (z_{-\mathbf{q}}^+ + \lambda_{-\mathbf{q}}^+) \rangle = \frac{k_B T}{2} (\mathbf{A}_{11}^{-1} + \mathbf{A}_{33}^{-1} + \mathbf{A}_{13}^{-1} + \mathbf{A}_{31}^{-1}) \quad (\text{D1})$$

$$= k_B T \frac{(\gamma_\lambda - \kappa_\theta) k_c q^4 + (\gamma_\lambda \kappa_\theta - k_\lambda k_c) q^2 - k_\lambda \kappa_\theta}{2\gamma_\lambda (\gamma_\lambda - \kappa_\theta) k_c q^6 + 2\kappa_\theta (\gamma_\lambda^2 - k_\lambda k_c) q^4},$$

$$\langle |\hat{p}_{\mathbf{q}}^\perp|^2 \rangle = \frac{k_B T}{2} (\mathbf{A}_{44}^{-1}) = \langle |\bar{p}_{\mathbf{q}}^\perp|^2 \rangle = \frac{k_B T}{2} (\mathbf{B}_{44}^{-1}) = \frac{k_B T}{2(\kappa_\theta + \kappa_{tw} q^2)},$$

$$\langle |\hat{p}_{\mathbf{q}}^\parallel|^2 \rangle = \langle (\hat{m}_{\mathbf{q}}^\parallel - i q \lambda_{\mathbf{q}}^+) (\hat{m}_{-\mathbf{q}}^\parallel + i q \lambda_{-\mathbf{q}}^+) \rangle = \frac{k_B T}{2} (\mathbf{A}_{22}^{-1} + i q \mathbf{A}_{23}^{-1} - i q \mathbf{A}_{32}^{-1} + q^2 \mathbf{A}_{33}^{-1}) \quad (\text{D2})$$

$$= k_B T \frac{(\gamma_\lambda - \kappa_\theta) k_c q^2 + \gamma_\lambda^2 - k_\lambda k_c}{2\gamma_\lambda (\gamma_\lambda - \kappa_\theta) k_c q^2 + 2\kappa_\theta (\gamma_\lambda^2 - k_\lambda k_c)},$$

$$\langle |t_{\mathbf{q}}|^2 \rangle = \langle (z_{\mathbf{q}}^- + \lambda_{\mathbf{q}}^-) (z_{-\mathbf{q}}^- + \lambda_{-\mathbf{q}}^-) \rangle = \frac{k_B T}{2} (\mathbf{B}_{11}^{-1} + \mathbf{B}_{31}^{-1} + \mathbf{B}_{13}^{-1} + \mathbf{B}_{33}^{-1}) \quad (\text{D3})$$

$$\begin{aligned}
&= \frac{k_B T \left\{ 4(\kappa_\theta - \gamma_\lambda) k_c^b q^4 + \left[-\frac{\Omega^2}{b_0^2} - \frac{4\kappa_\theta \Omega}{b_0} - 4\gamma_\lambda \kappa_\theta + 4 \left(\frac{k_A}{b_0} + k_\lambda \right) k_c^b \right] q^2 + 4 \left(\frac{k_A}{b_0} + k_\lambda \right) \kappa_\theta \right\}}{8\gamma_\lambda k_c^b (\kappa_\theta - \gamma_\lambda) q^6 - 2 \left[\gamma_\lambda \left(\frac{\Omega^2}{b_0^2} + 4\kappa_\theta \frac{\Omega}{b_0} + 4\gamma_\lambda \kappa_\theta \right) - 4k_\lambda \kappa_\theta k_c^b \right] q^4 - 2k_\lambda \frac{\Omega}{b_0} \left(\frac{\Omega}{b_0} + 4\kappa_\theta \right) q^2 + 8 \frac{k_A}{b_0^2} (\gamma_\lambda q^2 + k_\lambda) (k_c^b q^2 + \kappa_\theta)}, \\
\langle |\bar{p}_q^\parallel|^2 \rangle &= \langle (\bar{m}_q^\parallel - iq\lambda_q^-)(\bar{m}_{-q}^\parallel + iq\lambda_{-q}^-) \rangle = \frac{k_B T}{2} (\mathbf{B}_{22}^{-1} + iq\mathbf{B}_{23}^{-1} - iq\mathbf{B}_{32}^{-1} + q^2 \mathbf{B}_{33}^{-1}) \quad (D4) \\
&= \frac{k_B T \left\{ 4(\kappa_\theta - \gamma_\lambda) k_c^b q^6 - \left[\frac{\Omega^2}{b_0^2} + \frac{4\kappa_\theta \Omega}{b_0} + 4\gamma_\lambda^2 - 4 \left(\frac{k_A}{b_0} + k_\lambda \right) k_c^b \right] q^4 + 4 \left[(\gamma_\lambda + \kappa_\theta) \frac{k_A}{b_0} - \frac{\Omega k_\lambda}{b_0} \right] q^2 + 4k_\lambda \frac{k_A}{b_0^2} \right\}}{8\gamma_\lambda k_c^b (\kappa_\theta - \gamma_\lambda) q^6 - 2 \left[\gamma_\lambda \left(\frac{\Omega^2}{b_0^2} + \frac{4\kappa_\theta \Omega}{b_0} + 4\gamma_\lambda \kappa_\theta \right) - 4k_c^b k_\lambda \kappa_\theta \right] q^4 - 2k_\lambda \frac{\Omega}{b_0} \left(\frac{\Omega}{b_0} + 4\kappa_\theta \right) q^2 + 8 \frac{k_A}{b_0^2} (\gamma_\lambda q^2 + k_\lambda) (k_c^b q^2 + \kappa_\theta)}.
\end{aligned}$$

- ¹E. Browicz, *Zbl. Med. Wiss.* **28**, 625 (1890).
²F. Brochard and J. F. Lennon, *J. Phys. (France)* **36**, 1035 (1975).
³J. Israelachvili and H. Wennerström, *J. Phys. Chem.* **96**, 520 (1992).
⁴R. Lipowsky, *Nature (London)* **349**, 475 (1991).
⁵C. S. Peskin, G. M. Odell, and G. F. Oster, *Biophys. J.* **65**, 316 (1993).
⁶R. Bruinsma and P. Pincus, *Curr. Opin. Solid State Mater. Sci.* **1**, 401 (1996).
⁷R. Golestanian, M. Goulian, and M. Kardar, *Phys. Rev. E* **54**, 6725 (1996).
⁸W. Helfrich, *Z. Naturforsch. C* **28**, 693 (1973).
⁹P. B. Canham, *J. Theor. Biol.* **26**, 61 (1970).
¹⁰F. C. Frank, *Discuss. Faraday Soc.* **25**, 19 (1958).
¹¹R. Lipowsky and S. Grothhans, *Biophys. Chem.* **49**, 27 (1994).
¹²J. N. Israelachvili, *Intermolecular and Surface Forces* (Academic, New York, 1985).
¹³F. C. MacKintosh and T. C. Lubensky, *Phys. Rev. Lett.* **67**, 1169 (1991).
¹⁴M. Hamm and M. M. Kozlov, *Eur. J. Phys. E* **3**, 323 (2000).
¹⁵Y. Kozlovsky and M. M. Kozlov, *Biophys. J.* **82**, 882 (2002).
¹⁶P. I. Kuzmin, S. A. Akimov, Y. A. Chizmadzhev, J. Zimmerberg, and F. S. Cohen, *Biophys. J.* **88**, 1120 (2005).
¹⁷A. Kessel, N. Ben-Tal, and S. May, *Biophys. J.* **81**, 643 (2001).
¹⁸G. Khelashvili, G. Pabst, and D. Harries, *J. Phys. Chem. B* **114**, 7524 (2010).
¹⁹J. Aittoniemi, T. Róg, P. Niemelä, M. Pasenkiewicz-Gierula, M. Karttunen, and I. Vattulainen, *J. Phys. Chem. B* **110**, 25562 (2006).
²⁰S. May and A. Ben-Shaul, *Phys. Chem. Chem. Phys.* **2**, 4494 (2000).
²¹S. May and A. Ben-Shaul, *Biophys. J.* **76**, 751 (1999).
²²S. May, *Eur. Biophys. J.* **29**, 17 (2000).
²³S. May, *Langmuir* **18**, 6356 (2002).
²⁴M. Fošniarič, A. Iglič, and S. May, *Phys. Rev. E* **74**, 051503 (2006).
²⁵K. Bohinc, V. Kralj-Iglič, and S. May, *J. Chem. Phys.* **119**, 7433 (2000).
²⁶Y. Kozlovsky, J. Zimmerberg, and M. M. Kozlov, *Biophys. J.* **87**, 999 (2004).
²⁷J.-B. Fournier, *Eur. J. Phys. E* **11**, 261 (1999).
²⁸J.-B. Fournier, *Europhys. Lett.* **43**, 725 (1998).
²⁹B. West, F. L. H. Brown, and F. Schmid, *Biophys. J.* **96**, 101 (2009).
³⁰M. Hamm and M. M. Kozlov, *Eur. J. Phys. E* **6**, 519 (1998).
³¹S. Tristram-Nagle, R. Zhang, R. M. Suter, C. R. Worthington, W. J. Sun, and J. F. Nagle, *Biophys. J.* **64**, 1097 (1993).
³²T. C. Lubensky and F. C. MacKintosh, *Phys. Rev. Lett.* **71**, 1565 (1993).
³³C.-M. Chen, T. C. Lubensky, and F. C. MacKintosh, *Phys. Rev. E* **51**, 504 (1995).
³⁴K. Sengupta, V. A. Raghunathan, and Y. Hatwalne, *Phys. Rev. Lett.* **87**, 055705 (2001).
³⁵U. Seifert, J. Shillcock, and P. Nelson, *Phys. Rev. Lett.* **77**, 5237 (1996).
³⁶E. A. G. Aniansson, S. N. Wall, M. Almgren, H. Hoffmann, I. Kielmann, W. Ulbricht, R. Zana, J. Lang, and C. Tondre, *J. Phys. Chem.* **80**, 905 (1976).
³⁷T. J. McIntosh, S. Advani, R. E. Burton, D. V. Zhelev, D. Needham, and S. A. Simon, *Biochemistry* **34**, 8520 (1995).
³⁸A. Halperin and O. Mouritsen, *Eur. Biophys. J.* **34**, 967 (2005).
³⁹R. Goetz, G. Gompper, and R. Lipowsky, *Phys. Rev. Lett.* **82**, 221 (1999).
⁴⁰E. Lindahl and O. Edholm, *J. Chem. Phys.* **113**, 3882 (2000).
⁴¹E. Lindahl and O. Edholm, *Biophys. J.* **79**, 426 (2000).
⁴²S. J. Marrink and A. E. Mark, *J. Phys. Chem.* **105**, 6122 (2001).
⁴³S. W. Chiu, S. Vasudevan, E. Jakobsson, R. J. Mashl, and H. L. Scott, *Bio-phys. J.* **85**, 3624 (2003).
⁴⁴G. Brannigan and F. Brown, *Biophys. J.* **90**, 1501 (2006).
⁴⁵G. Brannigan, P. F. Phillips, and F. L. H. Brown, *Phys. Rev. E* **72**, 011915 (2005).
⁴⁶G. Brannigan, A. C. Tamboli, and F. L. H. Brown, *J. Chem. Phys.* **121** (2004).
⁴⁷M. J. Stevens, *J. Chem. Phys.* **121**, 11942 (2004).
⁴⁸I. R. Cooke, K. Kremer, and M. Deserno, *Phys. Rev. E* **72**, 011506 (2005).
⁴⁹W. K. den Otter, *J. Chem. Phys.* **123**, 214906 (2005).
⁵⁰J. Neder, B. West, P. Nielaba, and F. Schmid, *J. Chem. Phys.* **132**, 115101 (2009).
⁵¹B. West and F. Schmid, *Soft Matter* **6**, 1275 (2010).
⁵²E. R. May, A. Narang, and D. I. Kopelevich, *Phys. Rev. E* **76**, 021913 (2007).
⁵³E. R. May, A. Narang, and D. I. Kopelevich, *Mol. Simul.* **33**, 787 (2007).
⁵⁴F. M. Thakkar, P. K. Maiti, V. Kumaran, and K. G. Ayappa, *Soft Matter* **7**, 3963 (2011).
⁵⁵S. J. Marrink, J. H. Risselada, S. Yefimov, P. D. Tieleman, and A. H. de Vries, *J. Phys. Chem. B* **111**, 7812 (2007).
⁵⁶S. J. Marrink, A. H. de Vries, and A. E. Mark, *J. Phys. Chem. B* **108**, 750 (2004).
⁵⁷I. W. Stewart, *The Static and Dynamic Continuum Theory of Liquid Crystals: A Mathematical Introduction* (Taylor & Francis, London, 2004).
⁵⁸A. Imparato, *J. Chem. Phys.* **124**, 154714 (2006).
⁵⁹J.-B. Fournier and C. Barbetta, *Phys. Rev. Lett.* **100**, 078103 (2008).
⁶⁰W. Cai, T. C. Lubensky, P. Nelson, and T. Powers, *J. Phys. II* **4**, 931 (1994).
⁶¹O. Farago and P. Pincus, *Eur. Phys. J. E* **11**, 399 (2003).
⁶²O. Farago and P. Pincus, *J. Chem. Phys.* **120**, 2934 (2004).
⁶³J. Stecki, *J. Chem. Phys.* **125**, 154902 (2006).
⁶⁴F. Schmid, *Eur. Phys. Lett.* **95**, 28008 (2011).
⁶⁵S. A. Safran, *Statistical Thermodynamics of Surfaces, Interfaces and Membranes* (Westview Press, Boulder, CO, 1994).
⁶⁶N. G. V. Kampen, *Stochastic Processes in Physics and Chemistry* (Amsterdam, North Holland, 2007).
⁶⁷S. J. Plimpton, *J. Comput. Phys.* **117**, 1 (1995).
⁶⁸R. Goetz and R. Lipowsky, *J. Chem. Phys.* **108**, 7397 (1998).
⁶⁹P. J. Steinbach and B. B. Brooks, *J. Comput. Chem.* **15**, 667 (1994).
⁷⁰O. Farago, *J. Chem. Phys.* **119**, 596 (2003).
⁷¹D. Marsh, *Biochim. Biophys. Acta.* **1286**, 183 (1996).
⁷²E. Lindahl and O. Edholm, *J. Chem. Phys.* **113**, 3882 (2000).
⁷³M. Bhandarkar et al., *NAMD User's Guide. Version 2.7b2*, University of Illinois and Beckman Institute, Urbana, IL (2009), sec. 12.2.
⁷⁴A. Harasima, *Adv. Chem. Phys.* **1**, 203 (1958).
⁷⁵D. van der Spoel, E. Lindahl, B. Hess, G. Groenhof, A. E. Mark, and H. J. C. Berendsen, *J. Comput. Chem.* **26**, 1701 (2005).
⁷⁶H. J. C. Berendsen, D. van der Spoel, and R. van Drunen, *Comput. Phys. Commun.* **91**, 43 (1995).
⁷⁷B. Hess, C. Kutzner, D. van der Spoel, and E. Lindahl, *J. Chem. Theory Comput.* **4**, 435 (2008).
⁷⁸See <http://md.chem.rug.nl/cgmartini> to download pre-assembled bilayer coordinates and force field files.
⁷⁹S. O. H. Ollila, J. H. Risselada, M. Louhivuori, E. Lindahl, I. Vattulainen, and S. J. Marrink, *Phys. Rev. Lett.* **102**, 078101 (2009).

- ⁸⁰J. H. Irving and J. G. Kirkwood, *J. Chem. Phys.* **18**, 817 (1950).
- ⁸¹J. Sonne, F. Y. Hansen, and G. H. Peters, *J. Chem. Phys.* **122**, 124903 (2005).
- ⁸²W. H. Press, S. A. Teukolsky, W. T. Vetterling, and B. P. Flannery, *Numerical Recipes: The Art of Scientific Computing*, 3rd ed. (Cambridge University Press, Cambridge, England, 2007).
- ⁸³S. E. Feller and R. W. Pastor, *J. Chem. Phys.* **111**, 1281 (1999).
- ⁸⁴S. Shkulipa, *Computer Simulations of Lipid Bilayer Dynamics*, Ph.D. dissertation, University of Twente, The Netherlands, 2006.
- ⁸⁵Q. Waheed and O. Edholm, *Biophys. J.* **97**, 2754 (2009).
- ⁸⁶J. S. Rowlinson and B. Widom, *Molecular Theory of Capillarity* (Dover, New York, 2003).
- ⁸⁷G. Brannigan and F. L. H. Brown, *Biophys. J.* **92**, 864 (2007).
- ⁸⁸M. Watson and F. L. H. Brown, *Biophys. J.* **98**, L9 (2010).
- ⁸⁹E. G. Brandt, A. R. Braun, J. N. Sachs, J. F. Nagle, and O. Edholm, *Biophys. J.* **100**, 2104 (2011).
- ⁹⁰S. May, Y. Kozlovsky, A. Ben-Shaul, and M. M. Kozlov, *Eur. Phys. J. E* **14**, 299 (2004).
- ⁹¹M. Frigo and S. G. Johnson, *Proceedings of IEEE* **93**, 216 (2005).